


 Cite this: *RSC Adv.*, 2022, 12, 2843

# Integrated *in silico* – *in vitro* strategy for the discovery of potential xanthine oxidase inhibitors from Egyptian propolis and their synergistic effect with allopurinol and febuxostat†

 Dina S. Ghallab,<sup>a</sup> Eman Shawky,<sup>a</sup> <sup>a</sup> Ali M. Metwally,<sup>a</sup> Ismail Celik,<sup>b</sup> Reham S. Ibrahim <sup>‡\*a</sup> and Mohamed M. Mohyeldin <sup>‡a</sup>

Xanthine oxidase (XO) has been well-recognized as a validated target for the treatment of hyperuricemia and gout. Currently, there are two drugs in clinical use that shut down XO overactivity, allopurinol and febuxostat; however, detrimental side effects restrict their applications. Propolis is a unique natural adhesive biomass of structurally variable and biologically active metabolites that exert remarkable health benefits. Moreover, combination drug therapy has become a promising pharmacotherapeutic strategy directed for reformulating existing drugs into new combination entities with potentiating therapeutic impacts. In this study, computer-aided molecular docking and MD simulations accompanied by biochemical testing were used for mining novel pharmacologically active chemical entities from Egyptian propolis to combat hyperuricemia. Further, with a view to decrease the potential toxicity of synthetic drugs and enhance efficacy, propolis hits were subjected to combination analysis with each of allopurinol and febuxostat. More specifically, Glide docking was utilized for a structure-based virtual screening of in-house datasets comprising various Egyptian propolis metabolites. Rosmarinic acid, luteolin, techtochrysin and isoferulic acid were the most promising virtual hits. *In vitro* XO inhibitory assays demonstrated the ability of these hits to significantly inhibit XO in a dose-dependent manner. Molecular docking and MD simulations revealed a cooperative binding mode between the discovered hits and standard XO inhibitors within the active site. Subsequently, the most promising hits were tested in a fixed-ratio combination setting with allopurinol and febuxostat separately to assess their combined effects on XO catalytic inhibition. The binary combination of each techtochrysin and rosmarinic acid with febuxostat displayed maximal synergy at lower effect levels. In contrast, individually, techtochrysin and rosmarinic acid with allopurinol cooperated synergistically at high dose levels. Taken together, the suggested strategy seems imperative to ensure a steady supply of new therapeutic options sourced from Egyptian propolis to regress the development of hyperuricemia.

 Received 1st November 2021  
 Accepted 4th January 2022

DOI: 10.1039/d1ra08011c

[rsc.li/rsc-advances](http://rsc.li/rsc-advances)

## 1. Introduction

Xanthine oxidase (XO) is a highly versatile enzyme that is predominantly distributed throughout diverse mammalian tissues including the liver, gut, lung, kidney, heart, and brain, as well as the plasma.<sup>1</sup> XO is one of the rate-limiting enzymes involved in purine metabolism. Importantly, XO catalyzes the

sequential oxidative hydroxylation of hypoxanthine to uric acid *via* xanthine as an intermediate accompanied by the generation of two reactive oxygen species (ROS), hydrogen peroxide (H<sub>2</sub>O<sub>2</sub>), and superoxide anion (O<sup>2-</sup>).<sup>2</sup> These biochemical reactions can be illustrated in the schematic diagram depicted in Fig. 1.

Xanthine oxidoreductase (XOR) exists in two interconvertible forms; xanthine dehydrogenase (XDH) and XO.<sup>1</sup> Most XOR exists in its XDH form in the liver while being converted into the XO form under oxidative conditions.<sup>3</sup> The X-ray crystal structure of XO reveals a large homo-dimer with a molecular weight of 290 kDa. It belongs to a molybdo-flavoprotein family with each catalytically independent subunit-containing four redox-active sites: (a) one molybdo-pterin (Mo-pt) cofactor in the C-terminal domain, wherein the oxidation process of xanthine occurs reducing it from Mo(VI) to Mo(IV) by exploiting either NAD<sup>+</sup> or O<sub>2</sub>, (b) a pair of non-identical ferredoxin-like (2Fe-2S)

<sup>a</sup>Department of Pharmacognosy, Faculty of Pharmacy, Alexandria University, Alexandria 21521, Egypt. E-mail: rehamsaid84@yahoo.com; reham.abdelkader@alexu.edu.eg; Tel: +20-1223821098

<sup>b</sup>Department of Pharmaceutical Chemistry, Faculty of Pharmacy, Erziyes University, Kayseri 38039, Turkey

† Electronic supplementary information (ESI) available. See DOI: 10.1039/d1ra08011c

‡ Reham S. Ibrahim and Mohamed M. Mohyeldin contributed equally to the work.



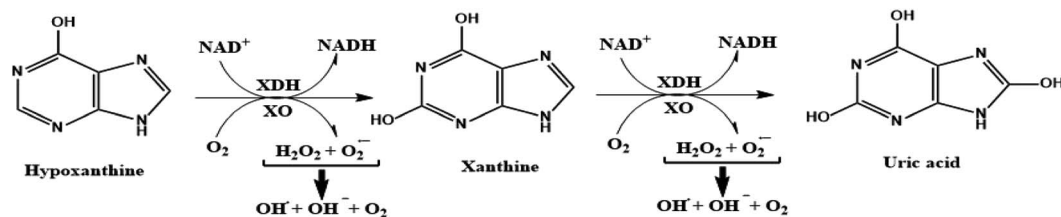


Fig. 1 Schematic diagram illustrating the oxidative hydroxylation of hypoxanthine to uric acid through xanthine as intermediate and the generation of reactive oxygen species in the purines metabolism.

centers in the N-terminal domain and, (c) one flavin adenine dinucleotide cofactor (FAD) located in the intermediate domain in which the reduction of NAD<sup>+</sup> to NADH takes place at the FAD site of XDH while that of O<sub>2</sub> to O<sub>2</sub><sup>-</sup> or hydrogen peroxide at the FAD site of XO.<sup>4</sup> These biochemical reactions usually proceed in a “ping-pong” manner.<sup>1</sup>

Overproduction or under-excretion of uric acid leads to an enhanced serum level of uric acid, which is termed hyperuricemia. Importantly, hyperuricemia is directly associated with elevated XO activity; it is potentially injurious and usually triggers numerous pathophysiological conditions including gout.<sup>5</sup> Gout is a common musculoskeletal pathology in which excessive levels of uric acid deposit as urate crystals in joints, resulting in painful acute gouty arthritis.<sup>6</sup> Moreover, gout is also linked with other deleterious conditions such as hypertension, diabetes mellitus and cardiovascular diseases.<sup>7</sup> Meanwhile, an elevated number of reactive oxygen species (ROS) generated by XO is also implicated in the development of inflammation, multiple cardiovascular attacks, renal hypoxia, ischemia-reperfusion injury and carcinogenesis.<sup>8</sup> Accordingly, xanthine oxidase has been recognized as a validated pharmacological target for the treatment of hyperuricemia and gout. Furthermore, XO inhibition has been considered as one of the best defensive approaches against hazardous oxidative stress due to free radicals. In this scenario, XO inhibitors markedly remain in the first-line as free radical scavengers.

Allopurinol is the first purine-based therapeutic option approved by the food and drug administration (FDA) for the clinical treatment of gout; it blocks the synthesis of uric acid by shutting down XO activity.<sup>9</sup> However, its prolonged use may cause undesirable side effects such as hypersensitivity problems, Stevens–Johnson syndrome, renal toxicity, liver necrosis and gastrointestinal distress.<sup>10</sup> Therefore, there is an immense need for evolving non-purine alternatives with potent XO inhibitory activity and better safety profile. Meanwhile, febuxostat has been launched in the US as a potent non-purine XO inhibitor, which has attracted worldwide attention.<sup>1</sup> Although febuxostat is a very clinically effective drug, its use is occasionally limited by some adverse effects including hypersensitive drug reactions.<sup>11</sup> Moreover, febuxostat has been lately restricted for broad use in various hyperuricemia-related diseases.<sup>12</sup> Recently, febuxostat has been issued a new boxed warning by the FDA cautioning that the drug may increase the risk of death from heart-related issues, or any other causes compared with allopurinol.<sup>13</sup> Hence, there is a continued need

to discover an expanded repertoire of novel XO inhibitors with an enriched pharmacological profile and diminished undesirable side effects.

The wonder plant-derived bee product, propolis (bee glue), has been traditionally used in complementary medicine since ancient times.<sup>14</sup> Propolis is a powerful resinous mixture that comprises multiple bioactive components including flavonoids, terpenes, alcohols, phenolic acids and their esters.<sup>15</sup> Due to its complex chemistry, propolis potentially exhibited various biological effects such as antioxidants, antimicrobial, anti-inflammatory, anticancer, hepatoprotective and anti-neurodegenerative activities.<sup>15</sup>

In fact, propolis has definitively a large variety of therapeutic properties, being broadly used since 300 years B.C. in folk medicine worldwide.<sup>16</sup> More specifically, poplar-type propolis has been traditionally used in gout- and arthritis-treatment practices in medieval Europe with satisfactory therapeutic outcomes.<sup>17</sup> Besides, *Populus nigra* is traditionally used to ameliorate several inflammatory-related pathologies primarily gouty arthritis, bronchitis and respiratory tract diseases.<sup>18</sup> Importantly, the inclusion of this wonderful bee product in food and food supplements as a safe complementary and alternative medicine has been readily approved by the United States Food and Drug Administration (FDA) and the Scientific Committee (SC) of the European Food Safety Authority (EFSA).<sup>19</sup>

The chemical variability and biological activities of propolis are markedly attributed to the plant origin, geographical locations and collecting season.<sup>20</sup> Egyptian propolis has recently drawn growing interest among chemists and biologists, both as a remedy and as a source of new pharmacologically active chemical entities owing to its diverse biomedical applications.<sup>21</sup> Propolis collected in Egypt has been demonstrated to have a chemical profile similar to the poplar-type propolis, which is rich in flavonoids and phenylpropanoids,<sup>22</sup> hence they can be utilized as attractive leads for the rational design of therapeutic xanthine oxidase inhibitors due to their beneficial antioxidant, anti-inflammatory, and micromolar inhibitory activities against xanthine oxidase.<sup>23</sup>

In the same context, previous studies have revealed that some flavonoids such as apigenin and luteolin, isolated from *Perilla frutescens*, act as potential XO competitive inhibitors with IC<sub>50</sub> values of  $(6.33 \pm 0.18) \times 10^{-6}$  and  $(8.21 \pm 0.77) \times 10^{-6}$  mol L<sup>-1</sup>, respectively, their inhibitory activities were superior to allopurinol [IC<sub>50</sub> =  $(13.16 \pm 0.72) \times 10^{-6}$  mol L<sup>-1</sup>].<sup>24</sup> In addition, pinobanksin and galangin were reported to exhibit



potent XO inhibitory potential in a dose-dependent and competitive manner.<sup>25</sup> Various *in vitro* kinetic studies have readily indicated that quercetin is a significant mixed-type inhibitor of xanthine oxidase with  $IC_{50}$  value of  $(2.92 \pm 0.03) \times 10^{-6} \text{ mol L}^{-1}$ .

Employing computational virtual screening approach can offer clear molecular insights into the ligand-binding mechanism by identification of the involved key amino acid residues, docking the molecules within the target protein, ranking hits according to their binding affinities, checking their physicochemical features and predicting their pharmacokinetics and toxic potential aimed at opening new avenues for the discovery of new potential drug-like candidates amenable for hit-to-lead design to satisfy unmet medical needs.<sup>26</sup>

Combination or multicomponent drug therapy has gained considerable attention as an effective approach in the management of chronic medical conditions, including rheumatoid arthritis, diabetes mellitus, Alzheimer's disease, malignancies, pulmonary disorders, cardiovascular diseases, pain, neurologic disorders, as well as HIV and other infectious diseases.<sup>27</sup> In this respect, multicomponent therapies exploit the chances for better efficacy, minimize adverse effects of each individual agent, and delay the emergence of drug resistance.<sup>28</sup> In addition, the reformulation of existing drugs into new combination products directed at multiple therapeutic targets acts as an attractive pharmacotherapeutic strategy for the pharmaceutical industry that is currently facing a diminution in the discovery and approval of novel molecular entities.<sup>29</sup> Currently, there are numerous preclinical-research articles on drug combinations in several disease settings including cancer, autoimmune, cardiovascular, metabolic, and neurological disorders to improve treatment response.<sup>30,31</sup> In the same context, a recent study revealed that the combined regimen of baicalein with allopurinol manifested a distinct synergistic effect against XO activity that could ultimately treat hyperuricemia, a pre-disposing factor of gout.<sup>32</sup>

In view of the aforementioned points, Egyptian propolis-derived phytoconstituents have been assessed in the present study for their XO inhibitory effects as well as the mechanisms underlying these effects using computer-aided molecular docking accompanied by further biochemical testing, in an attempt to discover novel candidates for the regulation of uric acid overproduction and its resulting complications. The resulting potential hits were also investigated for their XO enzyme suppressive effects when combined with allopurinol or febuxostat compared to a single compound treatment.

## 2. Materials and methods

### 2.1. Materials

XO enzyme (grade I, from bovine milk, approximately 10.4 units per mL) and xanthine substrate were purchased from Sigma Chemical Co. (St. Louis, MO, USA). Allopurinol, febuxostat, quercetin, rosmarinic acid, luteolin, kaempferol, isoferulic acid, genkwanin and techochrysin (analytical grade) were also obtained from Sigma-Aldrich Co. All other reagents and solvents used in the study were of analytical grade.

### 2.2. *In silico* docking studies

The Schrödinger Maestro 11.8 software package (LLC, New York, NY) was chosen for structure-based virtual screening as well as the prediction of the binding mode of the top-scoring constituents-XO complexes.

**2.2.1. Retrieval and preparation of ligand structures.** Based on a focused literature review targeting the chemical profile of Egyptian propolis, one hundred and fifty phytochemicals were retrieved for the generation of an in-house dataset of the most frequently occurring compounds in Egyptian propolis (Table S1†). The two-dimensional structures of most compounds along with those for the two reference drugs; febuxostat (CID 134018) and allopurinol (CID 2094) were obtained from PubChem database (<https://pubchem.ncbi.nlm.nih.gov/>) of the National Centre for Biotechnology Information in sdf file format. Unavailable structures in the PubChem database were searched in different literature and drawn using ChemDraw software (CambridgeSoft Corporation, Cambridge, USA) and saved as (.sdf) files.

After the dataset generation, the chemical structure of each compound was imported into the Maestro 11.8 panel interface (Maestro, version 11.8, 2018, Schrödinger, USA). The LigPrep 2.3 module (LigPrep, version 2.3, 2018, Schrödinger, USA) was implemented to generate the 3D structure and to search for different conformers. The OPLS (OPLS 2005, Schrödinger, USA) force field was implemented to geometrically optimize each ligand structure and compute partial atomic charges. Finally, since the chirality center of each ligand was not specified, 32 poses per ligand were generated with different steric features for subsequent docking studies.

**2.2.2. Retrieval and preparation of the target protein structure.** The X-ray crystal structure of bovine XO in the complex with the natural flavonoid inhibitor quercetin (PDB ID 3NVY), with the greatest resolution (2.0 Å) among the bovine XO proteins currently reported in the Protein Data Bank (PDB), was selected and retrieved from RCSB Protein Data Bank (<http://www.rcsb.org/pdb>). The target protein crystal structure was downloaded as pdb file and then prepared and optimized using the protein preparation wizard module implemented in the Schrödinger suite. Once the protein was optimized, hydrogen bonds and bond order were assigned using PROPKA (Jensen Research Group, Denmark). Zero-order bonds to metals and disulphide bonds were also created at pH 7.0. Furthermore, water molecules beyond 5 Å from the XO binding site were removed. Finally, energy minimization was implemented with a root mean square displacement (RMSD) value of 0.3 Å using an optimized potential for liquid simulation (OPLS 2005) force field.

**2.2.3. Grid box generation.** In order to carry out docking simulation on the prepared X-ray crystal structure of XO, the active site for docking was defined using a grid box with dimensions of  $15 \times 15 \times 15$  Å around the centroid of the co-crystallized ligand and a grid spacing of about 0.375 Å was set. This grid box size was used to perform binding interaction studies for the Egyptian propolis-derived molecules along with reference drugs on the XO crystal structure through molecular docking.



**2.2.4. Molecular docking.** The minimized and refined compounds from the LigPrep file were subjected to flexible docking using the Glide 11.8 module (Glide, version 11.8, 2018, Schrödinger, USA) in extra-precision (XP) mode, applying the Glide default parameters. Modeling scores were generated using the Glide-Dock program's empirical scoring functions. The 2D and 3D ligand-target protein interactions, including hydrogen bonds, ion-pair and hydrophobic interactions were displayed in the Maestro interface aiming at the investigation of the most favorable binding modes of ligands. After the docking simulation, docked compounds with the best scoring states (the lowest docking energy) were forwarded to further *in vitro* testing.

**2.2.5. Validation of docking process.** To ensure successful validation of the conducted docking protocol, a pose selection method was employed re-docking the co-crystallized ligand into its respective binding sites of 3NVY followed by calculating the root mean square deviation (RMSD) of the predicted pose to the co-crystallized one. The obtained values were less than 1 Å (a preselected cut-off/threshold value) revealing high docking accuracy.<sup>33</sup>

The constructed validation set comprising 30 molecules with experimentally verified activity against XO (Table S2†), together with 1000 decoys implanted at the Schrödinger suite were docked into 3NVY crystalline structure to judge the ability of the enzyme structure in discriminating XO inhibitors from decoys. Glide enrichment calculator with numerous validation parameters such as sensitivity, specificity, ROC, AUC-ROC, BEDROC and EF (at 2%, 5% and 10%) was employed to assess the accuracy of Glide docking in predicting geometric poses and scoring protein–ligand complexes.

**2.2.6. Molecular dynamics.** Molecular dynamics (MD) simulation was performed using Gromacs version 2020.4 (Groningen Machine for Chemical Simulations) to analyze the stability of XO and febuxostat, XO and techtochrysin, and XO and febuxostat + techtochrysin complexes.<sup>34</sup> Molecular dynamic system input files are generated by the CHARMM-GUI web server.<sup>35</sup> The topology file of the XO enzyme was created with the TIP3 water model with an amber FF119SB force field.<sup>36</sup> A distance of 15 Å from the surface of the protein center was maintained to define the rectangular system size for simulation. The system was neutralized by adding 0.15 M KCl. Molecular dynamics simulations were performed in the periodic boundary condition. The system was equilibrated with 0.1 ns NVT and 1 ns NPT stages at 1 atm pressure and 303.15 K temperature according to Nosé–Hoover<sup>37</sup> thermostat and Parrinello–Rahman<sup>38</sup> barostat. The 100 ns molecular dynamics simulation was performed with the leap-frog MD integrator. The Particle Mesh Ewald (PME) method and the linear constraint (LINCS) algorithm were performed to calculate long-range electrostatic interactions and covalent bond constraints, respectively. Trajectory analysis was performed with Gmx scripts, root mean square deviation (RMSD), root mean square fluctuation (RMSF), and the radius of gyration ( $R_g$ ) measurements. MD trajectory analysis results were created with PyMol Molecular Graphics System version 2.4.1 and graphics were created with GraphPad

Prism 8. Molecular mechanical Poisson–Boltzmann surface area (MM-PBSA) and coupling free energy calculation were performed using Rashmi Kumari's *g\_mmpbsa* package.<sup>39</sup>

### 2.3. Experimental treatments

Briefly, tested compounds were dissolved in 10% dimethyl sulfoxide (DMSO) as stock solutions ( $10.0 \times 10^{-3} \text{ mol L}^{-1}$ ), and then diluted to different concentrations according to the following protocol: all tested samples (10 mM) were quantitatively transferred into a 10 mL volumetric flask, dissolved in 10% dimethyl sulfoxide (DMSO) and the volume was adjusted to 10 mL with the same solvent, then 10  $\mu\text{L}$  portions from the prepared stock solutions were separately transferred into 10 mL volumetric flasks and the volume was adjusted to 10 mL using distilled water. Hence, (10  $\mu\text{M}$ ) stock solution for each tested sample was prepared. Finally, all stock solutions were diluted to the required concentrations with the buffer.

### 2.4. *In vitro* assay of xanthine oxidase inhibitory activity

The ability of *in silico* hits to inhibit the catalytic activity of xanthine oxidase was monitored spectrophotometrically (Hitachi U-2000 UV/visible spectrophotometer, UK) under aerobic conditions by continuously measuring uric acid formation using xanthine as a substrate at 295 nm according to the previously reported methods with slight modifications.<sup>23,24</sup> In brief, the assay mixture consisted of 1 mL of the test inhibitor solution, 1.9 mL of phosphate buffer (pH 7.5) and 0.1 mL of XO enzyme solution (0.24 units per mL in phosphate buffer, pH 7.5), which was prepared immediately before use. After pre-incubation at 37 °C for 15 min, the reaction was initiated by the addition of 1 mL of freshly prepared substrate solution (0.4 mM) into the mixture. The assay mixture was then incubated at 37 °C for 30 min. The enzyme reaction was stopped by adding 1 mL of hydrochloric acid (1 M) and the absorbance was measured at 295 nm using the UV/vis spectrophotometer. A blank solution was prepared in the same manner, but the enzyme solution was added to the assay mixture after adding 1 M HCl. The FDA-approved XO inhibitor, febuxostat (0.08  $\mu\text{M}$ ) was set up as a positive control. Each treatment was replicated twice, and XO activity was expressed as percent inhibition of xanthine oxidase. % inhibition was determined according to the following equation:

$$\frac{[1 - (\text{Abs}_{\text{Test inhibitor}} - \text{Abs}_{\text{positive control}})]}{(\text{Abs}_{\text{negative control}} - \text{Abs}_{\text{positive control}})} \times 100 \quad (1)$$

where  $\text{Abs}_{\text{negative control}}$  is the absorbance of the control solution without the tested samples,  $\text{Abs}_{\text{Test inhibitor}}$  is the absorbance of the tested samples solution and  $\text{Abs}_{\text{positive control}}$  is the absorbance of febuxostat solution that yields the maximal inhibitory effect.

Inhibitory potencies for the tested compounds were expressed as  $\text{IC}_{50}$  values (the concentrations causing the half-maximal inhibition) determined by fitting the experimental data to a dose-response nonlinear regression curve using GraphPad Prism software (Version 6.01).



**Table 1** Summary table showing the experimental data points of each individual agent tested in combination analysis at five representative dose levels

Effect level (EC <sub>x</sub> ) <sup>a</sup>	Dose (μM)			
	Techtchrysin	Rosmarinic acid	Febuxostat	Allopurinol
EC <sub>10</sub>	0.024	0.26	0.005	0.18
EC <sub>30</sub>	0.046	0.48	0.015	0.42
EC <sub>50</sub>	0.084	0.97	0.02	0.82
EC <sub>70</sub>	0.28	2.44	0.04	1.84
EC <sub>90</sub>	0.88	5.22	0.12	4.05

<sup>a</sup> EC<sub>10</sub>, EC<sub>30</sub>, EC<sub>50</sub>, EC<sub>70</sub> and EC<sub>90</sub>, are the doses of each individual agent required to induce 10, 30, 50, 70 and 90% inhibition of XO enzyme activity, respectively.

## 2.5. The study of synergistic inhibitory activity on XO enzyme

**2.5.1. The combination effects determined using the “fixed ratio” method.** *In silico* top-scoring compounds with the lowest IC<sub>50s</sub>; techtchrysin and rosmarinic acid were subjected to combination analysis with each of allopurinol and febuxostat, the widely used drugs in the clinical treatment of gout, to exploit the chances for better therapeutic efficacy, decreased potential toxicity of these synthetic drugs as well as delayed induction of drug resistance.

The XO inhibitory activity of the combination therapy was assayed using the same method as described in Section 2.4. Operationally, the doses of techtchrysin, rosmarinic acid, allopurinol and febuxostat exhibited the following effect levels of enzymatic activity reduction (10%, 30%, 50%, 70% and 90%) were redefined and summarized in Table 1.

The most active propolis hits; techtchrysin and rosmarinic acid were tested in a fixed-ratio combination setting with allopurinol or febuxostat to assess their combined effects on XO catalytic inhibition. Various published methodologies, including the median-effect analysis, isobologram, combination index, and dose reduction index analysis, were applied in an attempt to evaluate the nature of the proposed combinations in this study.

**2.5.1.1. The median-effect analysis approach.** Using the user-friendly CompuSyn software (Chou and Martin, 2005, CompuSyn Inc., USA), the sigmoidal dose-effect curve for every single agent and their binary combination was easily plotted and then transformed into their corresponding linear median-effect plots based on the median-effect equation,<sup>40</sup> derived from the general mass-action law principle. This principle provides a reasonable link between a single entity and multiple entities.<sup>41</sup> The median-effect equation (MEE) suggested by Chou (2006) can be itemized as follows<sup>42</sup>

$$\frac{Fa}{Fu} = \left( \frac{D}{D_m} \right)^m \quad (2)$$

where  $D$  is the dose of a drug,  $D_m$  is the median-effect dose (analogous to ED<sub>50</sub>) that declines the enzymatic activity by 50%,  $fa$  is the fraction affected by  $D$  (*i.e.*, percentage effect/100),  $fu$  is the fraction unaffected ( $fu = 1 - fa$ ),  $m$  is the slope of the

median-effect plot denoting the shape of the dose-effect curve eqn (2) can be rearranged into:

$$\log\left(\frac{fa}{fu}\right) = m \log(D) - m \log(D_m) \quad (2')$$

In the median-effect plot,  $y = \log(fa/fu)$  versus  $x = \log(D)$ ,  $\log(D_m)$  is the  $x$ -intercept. The conformity of the data to the mass-action principle can be manifested by the linear correlation coefficient ( $r$ ) of the median-effect plot, which is usually  $>0.97$  for *in vitro* experiments.<sup>43</sup>

**2.5.1.2. Isobolographic analysis.** Dose-normalized isobolograms were generated using the computer program CompuSyn (Chou and Martin, 2005, CompuSyn Inc., USA) to provide a fundamental basis for illustrating the dose-dependent interaction of combined drugs at various effect levels. The combination effect could be greater, equal to, or smaller than would have been expected from individual agents.<sup>41</sup>

Operationally, isobologram is a two-coordinate plot with each coordinate representing the concentration of drugs A and B, respectively. The concentrations of both drugs A and B needed to yield a particular effect  $x$  (*e.g.*, IC<sub>50,A</sub> and IC<sub>50,B</sub> when  $x = 50\%$ ), when applied as single drugs, were placed on the  $x$  and  $y$ -coordinates, respectively. The diagonal line of additivity was created by connecting these two points (*e.g.*, (IC<sub>50,A</sub>, 0) and (0, IC<sub>50,B</sub>) for a 50% effect isobologram plot). Following that, the concentrations of A and B, which have been used in the combination study to provide the same effect  $x$  (*e.g.*  $x = 50\%$ ), were represented in the same plot as a by point (CA,  $x$ , CB,  $x$ ). Combination data points depicted above, on or below the additivity line indicated antagonism, additivity, or synergy, respectively.<sup>44</sup>

**2.5.1.3. Combination index analysis.** The isobologram-combination index equation (CI) merging with the median-effect equation provides a quantitative measurement of the extent of interaction of combined drugs at a series of effect levels. CI numerical values were automatically calculated using CompuSyn software (Chou and Martin, 2005, CompuSyn Inc., USA) according to the following formula<sup>45</sup>

$$CI = \frac{Da}{(Dx)_a} + \frac{Db}{(Dx)_b} \quad (3)$$



Table 2 Summary table showing various molar concentrations and ratios of both febuxostat and techtochrysin in multiple-ratio combination analysis design<sup>a</sup>

Molar concentration ratios		Techtochrysin					
		0	0.021	0.042	0.084	0.168	0.336
Febuxostat	0	0%	8%	22%	50%	64%	76%
	0.0025	6%	1 : 8.4	1 : 16.8	1 : 33.6	1 : 67.2	1 : 134.4
	0.005	10%	1 : 4.2	1 : 8.4	1 : 16.8	1 : 33.6	1 : 67.2
	0.01	24%	1 : 2.1	1 : 4.2	1 : 8.4	1 : 16.8	1 : 33.6
	0.02	50%	1 : 1.05	1 : 2.1	1 : 4.2	1 : 8.4	1 : 16.8
	0.04	70%	1 : 0.525	1 : 1.05	1 : 2.1	1 : 4.2	1 : 8.4

<sup>a</sup> The molar febuxostat–techtochrysin ratios 1 : 2.1, 1 : 4.2 (IC<sub>50</sub> : IC<sub>50</sub> ratio), 1 : 8.4, 1 : 16.8, and 1 : 33.6 are indicated in pink, green (IC<sub>50</sub> : IC<sub>50</sub> ratio), red, orange and grey.

where  $(Dx)a$  and  $(Dx)b$  are the doses of every single compound required to produce  $x$  effect level of enzymatic activity reduction, and  $Da$  and  $Db$  are the doses of the two compounds in combination that produce the same effect. CI was used to assess whether combinations at effect  $x$  yield synergistic (CI < 0.9), additive (CI = 0.9–1.1), or antagonistic (CI > 1.1) effect.<sup>43</sup>

Meanwhile, combination index (fa–CI) plots were automatically generated using CompuSyn software (CompuSyn Inc., 2005) by plotting combination indices against a series of effect levels. The fa–CI plot represents an effect-oriented plot that simply displays the kind of interaction; synergism, antagonism, or additive effect, as a function of the effect level or potency (fa) of certain combined drugs on the enzyme.<sup>45</sup> It is worth noting that the effect-oriented plot (fa–CI) and the dose-oriented isobologram are two sides of the same coin; each of them is based on MEE (eqn (2) and (2')) and hence provides an identical conclusion of synergism or antagonism.

**2.5.1.4. Dose reduction index (DRI) analysis.** The dose reduction index (DRI) of two-compound combinations indicates how many-fold dose-reduction is achieved for each compound in their synergistic combination, as compared with the doses of each drug alone, to produce the same enzymatic activity reduction effect (fa).<sup>46</sup>

DRI was automatically calculated using CompuSyn software by applying the following formula:<sup>47</sup>

A fold change of DRI > 1 is useful as it implies a decline of doses of combined agents while retaining the same

Additional to the above combination analysis approaches and with our aim of exploring the most efficacious combination therapeutics with enriched pharmacological potency and better safety profile, optimizing the synergistic dose ratios is considered a crucial factor in a combination regimen to gain the full benefits of multicomponent therapies.<sup>47</sup> For this purpose, the two combined agents with the highest CI and DRI; techtochrysin and febuxostat, were subjected to further combination analysis using the multiple ratio design to readily optimize the combination dose ratio and provide a more complete description of their joint inhibitory effect so that their synergism can be exploited effectively. The XO inhibitory activity of the proposed combinations was assessed using the same method as described in Section 2.4. Operationally, XO enzyme was treated with five different doses of febuxostat each in combination with five different concentrations of techtochrysin. Techtochrysin was applied at a concentration approximately equal to its IC<sub>50</sub> value as well as at concentrations within two-fold increments above or below its IC<sub>50</sub> as summarized in Table 2. Whereas, the experimental doses of febuxostat ranged from 0.0025 to 0.04 μM, including its IC<sub>50</sub>, approximately three-fold increments below its IC<sub>50</sub> value and one-fold increment above this value (Table 2). This protocol yielded a total of 25 different techtochrysin/febuxostat combinations representing nine different molar concentration ratios for both drugs. Simultaneously, each drug was used alone at these concentrations as controls, and all data points were repeated twice. The reduction of the XO catalytic ability was monitored

$$DRI = \frac{EDX \text{ of compound alone}}{EDX \text{ of the compound in combination with combination partner}} \quad (4)$$

effectiveness. Such favorable dose-reduction whilst maintaining the same therapeutic efficacy could result in an improvement of the potential toxicity profile to the host in clinical settings.

**2.5.2. The combination effects determined using the “multiple ratio” design supported with curve shift analysis.**<sup>47</sup>

spectrophotometrically at 295 nm. CI and DRI values were determined for each combination.

**2.5.3. Curve-shift analysis.** The curve-shift analysis provides a direct and simultaneous comparison of the dose-response curves of the investigated single agents as well as



combination treatments in the same plot and visually predicts the kind of drug–drug interaction.<sup>48</sup> A curve-shift diagram was established for each teichochrysin and febuxostat and their combination at 1 : 4.2 ( $IC_{50} : IC_{50}$  molar ratio) and other different molar-based ratios (1 : 2.1, 1 : 8.4, 1 : 16.8, and 1 : 33.6). Each agent alone or their combined concentrations ( $IC_{50} : IC_{50}$  ratio or other indicated ratios) were normalized to their respective single-agent  $IC_{50}$  and referred to as  $IC_{50}$  equivalent-concentrations ( $IC_{50}$  eq).  $IC_{50eq}$  of individual and combined drugs were calculated using the following formula:<sup>47</sup>

$$IC_{50eq} = \frac{C_{A,X}}{IC_{50A}} + \frac{C_{B,X}}{IC_{50B}} \quad (5)$$

where  $IC_{50A}$  and  $IC_{50B}$  are the  $IC_{50}$  values of drugs A and B, respectively.  $C_{A,X}$  and  $C_{B,X}$  are the concentrations of drugs; A and B are required to produce  $x\%$  effect. For individual compounds, either  $C_{A,X}$  or  $C_{B,X}$  in eqn (5) becomes zero.

Following that,  $IC_{50}$  eq data of individual agents; teichochrysin and febuxostat, as well as their combined treatments at different molar concentration ratios were graphed in the same plot against their corresponding inhibitory effect levels from 0–100% ( $Fa \times 100$ ) using GraphPad Prism. Such simultaneous presentation of these concentration-effect curves would easily illustrate that lower drug concentrations are needed to attain any particular XO inhibitory effect relative to individual agents. Synergistic combinations will exhibit lower  $IC_{50eq}$  values relative to single agents ( $IC_{50eq}$  values of one) to achieve any given effect. This is visually represented in a leftward shift of the combination trendlines relative to the dose-response curves of the single agents indicating synergy. In contrast, a rightward shift of concentration-effect curves for combinations can be interpreted as antagonism.<sup>47</sup>

## 2.6. Statistical analysis

The results are presented as the means  $\pm$  standard deviation (SD) of at least three independent experiments and analyzed by one-way (ANOVA) followed by Tukey post hoc test for single measurements,  $p < 0.001$  was considered statistically significant. Statistical analysis was performed using GraphPad Prism (GraphPad, version 6.01) software and the Computer program CompuSyn (Chou and Martin, 2005, CompuSyn Inc., USA). The  $IC_{50}$  values were calculated using a non-linear regression curve fitting analysis using GraphPad Prism software version 6.01 (La Jolla, CA, USA).

## 3. Results and discussion

### 3.1. Molecular docking studies on the database

**3.1.1. Virtual screening of Egyptian propolis small library and molecular docking studies.** In this study, a virtual screening campaign is described to identify new natural products that inhibit the XO catalytic activity from Egyptian propolis. The small in-house generated dataset consisted of one hundred and fifty natural metabolites from Egyptian propolis along with the two reference drugs; allopurinol and febuxostat. Molecular docking has been chosen as a suitable approach for virtual screening since several crystal structures for human and bovine XO have been published, with and without ligands. To mimic *in vitro* testing, the primary target crystal structure used was that of bovine XO co-crystallized with quercetin (PDB ID 3NVY), which shows 90% overall sequence homology with human xanthine oxidase.<sup>49</sup>

Protein visualization revealed a homodimer composed of three chains each with a tertiary structure of two domains, an alpha-beta roll and a mainly alpha orthogonal bundle. Xanthine

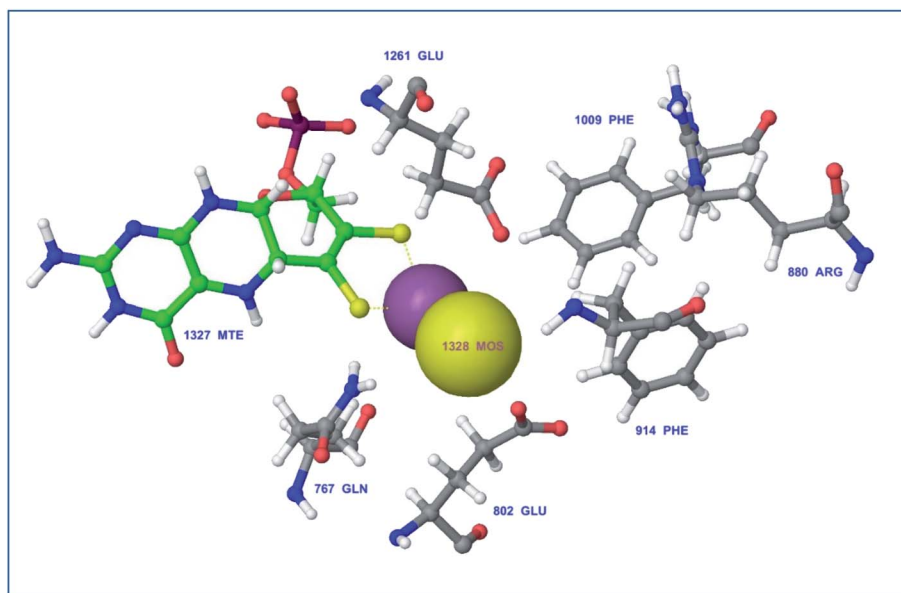


Fig. 2 Catalytic amino acid residues in the active site of xanthine oxidase (PDB ID 3NVY). Amino acid residues are shown in grey color and labeled with names and positions. Molybdopterin (Mo) cofactor is shown in green color (ball and stick model) with Mo atoms in yellow & violet (space-filling (CPK) model).





**Table 3** Virtual screening results against bovine XO crystal structure (3NYY): names and chemical structures of top 20 scoring hits and two reference drugs, their docking scores after molecular docking simulations and types of binding interactions between ligands and key amino acid residues in the binding site of XO

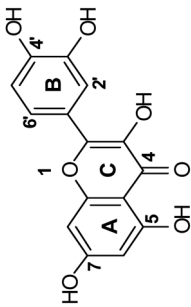
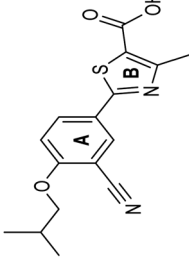
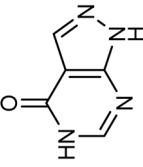
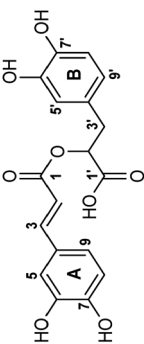
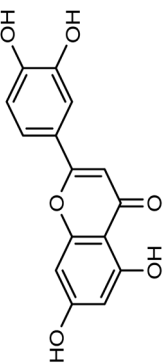
Rank	Hit name & chemical structure	Docking score	Type of interaction <sup>a</sup>	Amino acid (ligand functional group) involved in interaction
—	 <b>Quercetin (Co-crystallized ligand)</b>	−9.993	Hb (side chain) π-π stacking Hydrophobic	SER876 (3'-OH), ARG880 (7-OH), THR1010 (7-OH), GLU802 (3-OH) ARG880 (ring A), PHE1009 (ring A), PHE914 (ring A) PHE1013 (ring B), LEU 1014 (ring B), LEU873 (ring B)
—	 <b>Febuxostat (Reference Drug)</b>	−10.039	Hb (backbone and side chain) Hydrophobic π-π stacking Salt bridge	ARG880 (C=O), THR1010 (COO <sup>-</sup> ), ASN768 (CN) LEU648 (isobutyl), LEU873 (ring A) PHE1009 (ring B), PHE914 (ring B) ARG880 (COO <sup>-</sup> )
—	 <b>Allopurinol (Reference Drug)</b>	−4.975	Hb (backbone and side chain) π-π stacking	THR1010 (C=O & pyrimidine NH), ARG880 (C=O) ARG880 (pyrazole), PHE1009 (pyrazole), PHE914 (pyrazole)
1	 <b>Rosmarinic acid</b>	−10.390	Hb (side chain) π-π stacking Hydrophobic Salt bridge	SER876 (6' & 7'-OH), ARG880 (7-OH), THR1010 (7-OH), ASN768 (1'-C=O) ARG880 (ring A), PHE1009 (ring A), PHE914 (ring A) LEU648 (ring B), PHE649 (ring B) LYS771 (1'-COO <sup>-</sup> )
2	 <b>Luteolin</b>	−9.887	Hb (side chain) Hydrophobic π-π stacking	THR1010 (7-OH), ARG880 (7-OH) LEU648 (ring B), PHE1013 (ring B) PHE1009 (ring A), PHE914 (ring A), ARG880 (ring A)
3		−9.563	Hb (backbone and side chain)	THR1010 (5-OH), ARG880 (5-OH), VAL1011 (C=O)



Table 3 (Contd.)

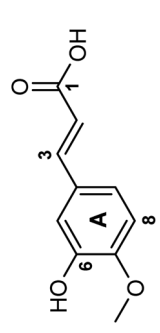
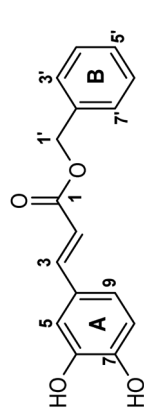
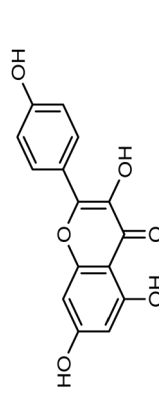
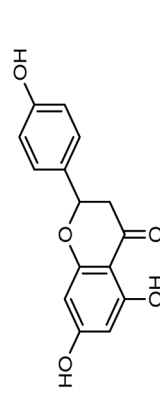
Rank	Hit name & chemical structure	Docking score	Type of interaction <sup>a</sup>	Amino acid (ligand functional group) involved in interaction
4	 <p><b>Techtochrysin</b></p>  <p><b>Isoferulic acid</b></p>	-9.557	<p>Hb (backbone and side chain) Salt bridge Hydrophobic</p>	<p>ARG880 (C=O), SER876 (6-OH), THR1010 (COO<sup>-</sup>) ARG880 (COO<sup>-</sup>) PHE1013 (ring A), LEU1014 (ring A)</p>
5	 <p><b>Phenethyl-trans-caffeate (CAPA)</b></p>	-9.474	<p>Hb (side chain) <math>\pi</math>-<math>\pi</math> stacking Hydrophobic <math>\pi</math>-cation</p>	<p>THR1010 (6-OH), ARG880 (7-OH) PHE1009 (ring A), PHE914 (ring A) VAL1011 (ring B), PHE1013 (ring B), LEU1014 (ring B) LYS771 (ring B)</p>
6	 <p><b>Benzyl-trans-caffeate</b></p>	-9.343	<p>Hb (side chain) <math>\pi</math>-<math>\pi</math> stacking Hydrophobic</p>	<p>THR1010 (6-OH), ARG880 (7-OH) PHE1009 (ring A), PHE914 (ring A) LEU648 (benzyl moiety), PRO1076 (ring B), ALA1078 (ring B)</p>
7	 <p><b>Kaempferol</b></p>	-9.289	<p>Hb (side chain) <math>\pi</math>-<math>\pi</math> stacking Hydrophobic</p>	<p>THR1010 (7-OH), ARG880 (7-OH), GLU802 (3-OH) PHE1009 (rings A &amp; C), PHE914 (rings A &amp; C) LEU873 (ring B), LEU1014 (ring A)</p>
8	 <p><b>Naringenin</b></p>	-9.252	<p>Hb (backbone and side chain) <math>\pi</math>-<math>\pi</math> stacking Hydrophobic</p>	<p>THR1010 (C=O), VAL1011 (C=O), ARG880 (5-OH), ALA1079 (7-OH) PHE1009 (ring A), PHE914 (ring A) LEU1014 (ring B), ALA 1078 (ring A)</p>
9		-9.221	<p>Hb (backbone and side chain)</p>	<p>THR1010 (5-OH), ARG880 (5-OH), VAL1011 (C=O)</p>





Table 3 (Contd.)

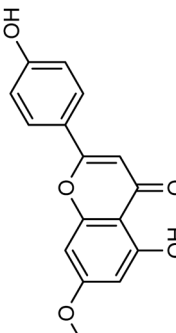
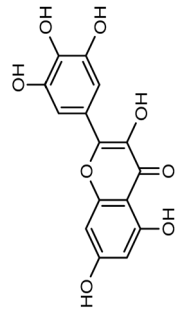
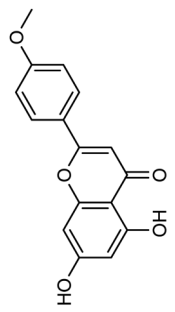
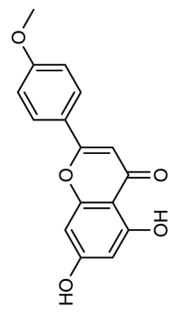
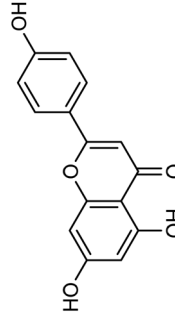
Rank	Hit name & chemical structure	Docking score	Type of interaction <sup>a</sup>	Amino acid (ligand functional group) involved in interaction
	 <p><b>Genkwainin</b></p>		Hydrophobic $\pi$ - $\pi$ stacking	LEU1014 (ring B) PHE1009 (rings A & C), PHE914 (rings A & C)
10	 <p><b>Myricetin</b></p>	-9.158	Hb (side chain) $\pi$ - $\pi$ stacking Hydrophobic	THR1010 (7-OH), ARG880 (7-OH), GLU802 (3-OH) PHE1009 (rings A & C), PHE914 (rings A & C) LEU648 (ring B), PHE649 (ring B)
11	 <p><b>Acacetin</b></p>	-9.145	Hb (side chain) $\pi$ - $\pi$ stacking Hydrophobic	THR1010 (7-OH), ARG880 (7-OH) PHE1009 (rings A & C), PHE914 (rings A & C) LEU648 (ring B), PHE649 (ring B), LEU873 (ring B), VAL1011 (ring B), PHE1013 (ring B), LEU1014 (ring B)
12	 <p><b>Acacetin</b></p>	-8.981	Hb (side chain) $\pi$ - $\pi$ stacking Hydrophobic	THR1010 (7-OH), ARG880 (7-OH) PHE1009 (rings A & C), PHE914 (rings A & C) LEU648 (ring B), PHE649 (ring B), LEU873 (ring B), VAL1011 (ring B), PHE1013 (ring B), LEU1014 (ring B)
13	 <p><b>Apigenin</b></p>	-8.857	Hb (side chain) $\pi$ - $\pi$ stacking Hydrophobic	THR1010 (7-OH), ARG880 (7-OH) PHE1009 (rings A & C), PHE914 (rings A & C) VAL1011 (ring B), PHE1013 (ring B), PHE1005 (ring A)

Table 3 (Contd.)

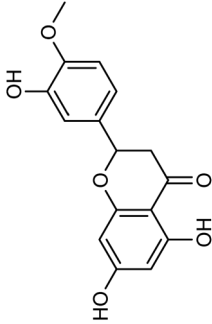
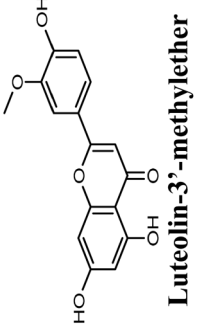
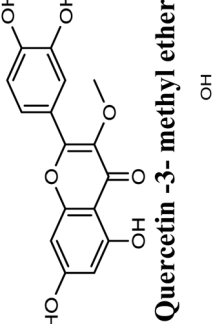
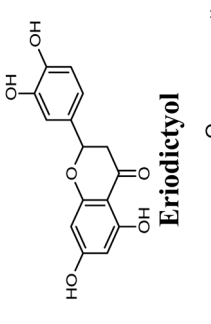
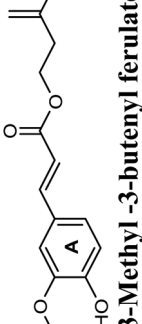


Rank	Hit name & chemical structure	Docking score	Type of interaction <sup>a</sup>	Amino acid (ligand functional group) involved in interaction
14	 <p><b>Hesperetin</b></p>	-8.842	Hb (side chain) $\pi$ - $\pi$ stacking Hydrophobic	THR1010 (7-OH) PHE1009 (ring A), PHE914 (ring A) LEU648 (ring B), PHE1013 (ring B), LEU1014 (ring B), PRO1076 (ring B)
15	 <p><b>Luteolin-3'-methyl ether</b></p>	-8.791	Hb (side chain) $\pi$ - $\pi$ stacking Hydrophobic	THR1010 (7-OH), ARG880 (7-OH) PHE1009 (rings A & C), PHE914 (rings A & C) Pro1076 (ring B), VAL1011 (ring B), PHE1013 (ring B), LEU 1014 (ring B)
16	 <p><b>Quercetin-3-methyl ether</b></p>	-8.775	Hb (side chain) $\pi$ - $\pi$ stacking Hydrophobic	SER876 (3'-OH), THR1010 (7-OH), ARG880 (7-OH) PHE1009 (rings A & C), PHE914 (ring A) PRO1076 (3-OCH <sub>3</sub> ), ALA1078 (3-OCH <sub>3</sub> ), ALA1079 (3-OCH <sub>3</sub> ), PHE649 (ring B)
17	 <p><b>Eriodictyol</b></p>	-8.660	Hb (side chain) $\pi$ - $\pi$ stacking Hydrophobic	THR1010 (7-OH) PHE1009 (ring A), PHE914 (ring A) PHE649 (ring B), VAL1011 (ring B), PHE1013 (ring B), LEU1014 (ring B)
18	 <p><b>3-Methyl-3-butenyl ferulate</b></p>	-8.616	Hb (side chain) $\pi$ - $\pi$ stacking Hydrophobic	ARG880 (7-OH, 6-OCH <sub>3</sub> ), THR1010 (7-OH) PHE1009 (ring A), PHE914 (ring A) LEU648 (butenyl group), PHE1013 (butenyl group), LEU1014 (butenyl group)





Table 3 (Contd.)

Rank	Hit name & chemical structure	Docking score	Type of interaction <sup>a</sup>	Amino acid (ligand functional group) involved in interaction
19	 <p><b>Stearic acid</b></p>	-8.583	Hb (backbone and side chain) Salt bridge Hydrophobic	ARG880 (C=O), THR1010 (C=O) ARG880 (COO <sup>-</sup> ) LEU648, PHE649, PHE1009, PHE1013, LEU1014, MET1118 (long 18-carbon chain) ARG880 (C=O), THR1010 (COO <sup>-</sup> ) ARG880 (COO <sup>-</sup> ) LEU648, PHE914, VAL1011, PHE1013, LEU1014 (long 16-carbon chain)
20	 <p><b>Palmitic acid</b></p>	-8.484	Hb (backbone and side chain) Salt bridge Hydrophobic	

<sup>a</sup> Hb denotes hydrogen bonding interaction,  $\pi$ - $\pi$  stacking denotes  $\pi$ - $\pi$  stacking.

oxidase has two distinct substrate-binding sites; (a) molybdenum molybdopterin (Mo-pt) active site in which the catalytic oxidation of xanthine occurs reducing it from Mo(vi) to Mo(iv) and (b) flavin adenine dinucleotide (FAD) center wherein the substrate oxygen is reduced with transferred electrons generating O<sub>2</sub><sup>-</sup> radical or hydrogen peroxide (H<sub>2</sub>O<sub>2</sub>).<sup>1</sup> The Mo center is characterized by critical amino acids including ARG880, PHE1009, PHE914, GLU802, ASN768, THR1010, VAL1011, LEU873, and GLU1216, aligning a water channel near the molybdenum atom of the Mo-pt cofactor (Fig. 2), and they were proven to play pivotal roles in the catalytic hydroxylation of the substrate.<sup>1</sup> Catalytic inhibitors usually bind to the Mo-pt active site forming multiple interactions with its key amino acid residues involved in catalysis. This will in turn completely block the water channel leading to the molybdenum center and its surrounding space and hinder the binding of xanthine, preventing its oxidation.<sup>50</sup> Accordingly, the binding site of the co-crystallized ligand; quercetin, which involved ARG880, PHE1009, PHE914 and GLU802 was chosen for docking simulation (PDB ID 3NVY, Fig. 2).

A test or a training run was performed using two marketed XO inhibitor drugs; allopurinol and febuxostat in addition to the co-crystallized ligand quercetin due to its well-documented XO inhibitory activity.<sup>51</sup>

The test run has been applied in order to validate the virtual screening protocol and ensure its efficiency. The test set was prepared and docked into the chosen XO crystal structure 3NVY using Glide XP (Schrödinger, USA). The three compounds in the test set were docked successfully, suggesting the validity of the implemented docking parameters (Table 3 and Fig. S1-S3<sup>†</sup>). The bound conformation of the co-crystal ligand; quercetin was generated with a good RMSD of 0.3 Å, showing the robustness of the docking protocols. As expected, febuxostat and quercetin demonstrated strong binding affinities with docking scores of -10.039 and -9.993, respectively (Table 3). Both compounds were able to fill the water channel near the molybdenum atom of the Mo-pt cofactor and thus inhibited enzyme activity by obstructing the substrate-binding (Fig. S1 and S2<sup>†</sup>). In contrast, allopurinol exhibited much lower binding affinity with a docking score of -4.957, despite satisfying some critical interactions with key amino acids in the active site (Table 3 and Fig. S3<sup>†</sup>). Such a low docking score of allopurinol could be attributed to the imperfect filling of the crucial hydrophobic space within the substrate entering channel near the molybdenum atom of the Mo-pt cofactor, leading to a serious energy penalty affecting the allopurinol's overall binding affinity. It is important to point out that allopurinol, unlike febuxostat and quercetin, is further hydroxylated by XO to give oxipurinol, the actual potent inhibitor of XO in biological settings, which in turn tends to bind covalently to the reduced molybdenum ion Mo(iv) of the enzyme and inhibits catalysis.<sup>52</sup> Importantly, oxipurinol exhibited only weak inhibition of the enzyme without this covalent bond.<sup>53</sup> This could explain the relatively low docking score of allopurinol in the training set *in silico* results and suggest the validity of the implemented scoring functions.

The in-house compound set was prepared and docked into the same XO crystal structure 3NVY applying the same docking

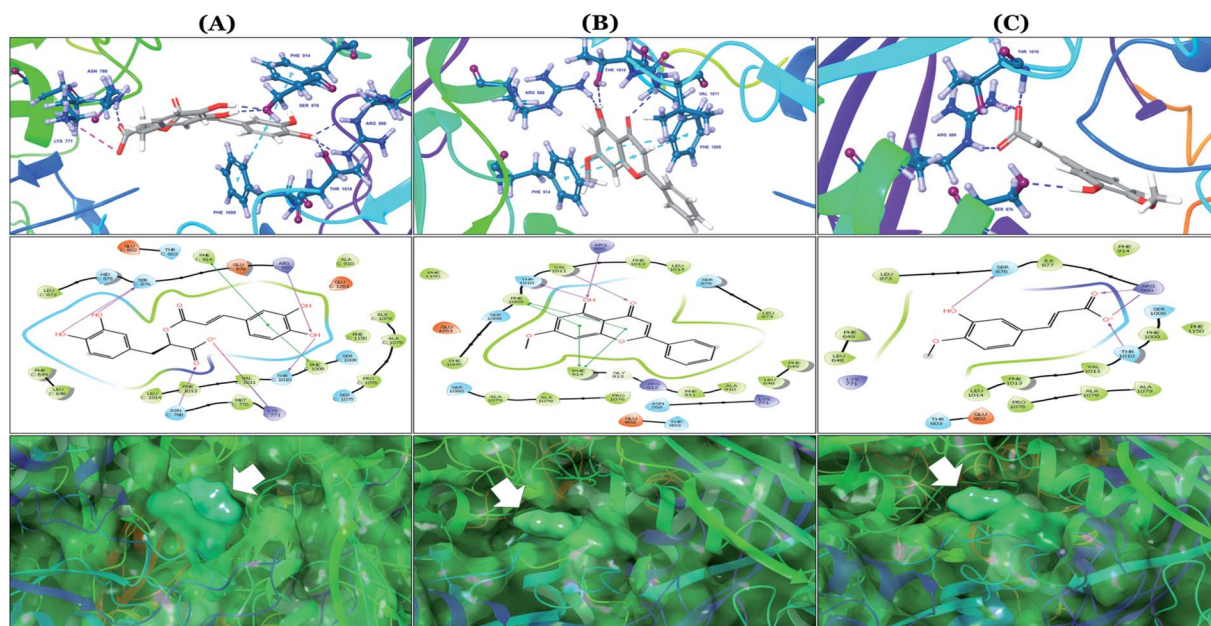


**Fig. 3** *In silico* binding poses of (A) rosmarinic acid, (B) techtochrysin, and (C) isoferulic acid interacting with XO active site's amino acid residues (PDB ID 3NVY). Upper panel: important interactions of potential hits along with the corresponding amino acids at the XO binding site, the protein is shown in three-dimensional cartoon presentation. Blue dotted lines indicate hydrogen bonds while light blue dotted lines show pi-pi stacking interactions. Magenta dotted lines indicate salt bridges in 3D view. Middle panel: the two-dimensional ligand interaction diagrams (LID) of potential hits at the XO binding site are shown. Magenta solid arrows indicate hydrogen bonds (backbone) while magenta dotted arrows denote hydrogen bonds (side chain). Green & purplish red solid lines represent pi-pi stacking interactions and salt bridges, respectively. Lower panel: the transparent protein surface, in aquamarine color, and the solid hits surface, in spring green color marked with white arrows.

parameters used for the test set and binding poses were saved. Following that, potential hits were ranked according to their extra precision docking scores and the results for the top twenty virtual hits are demonstrated in Table 3. The primary hit list resulting herein consisted of a compilation of 20 natural products belonging to different chemical classes including flavonoids (*e.g.* techtochrysin), phenolic acids (*e.g.* isoferulic acid), phenolic esters (*e.g.* 3-methyl-3-butenyl ferulate), phenolic esters with a free carboxylic acid group (*e.g.* rosmarinic acid), and long-chain saturated fatty acids (*e.g.* stearic acid). For instance, Fig. S4† shows the docking model of techtochrysin in the co-crystal structure of quercetin bound to XO (PDB ID 3NVY). Techtochrysin almost overlaid quercetin, the original co-crystallized ligand, satisfying the same critical interactions within the Mo-pt center (Fig. S4†).

Docking and ranking results revealed that rosmarinic acid, luteolin, techtochrysin and isoferulic acid had the lowest binding energies and the strongest binding affinities with docking scores of  $-10.390$ ,  $-9.887$ ,  $-9.563$  and  $-9.557$ , respectively (Table 3). Among the primary hit list, the natural flavonoid luteolin has been previously reported to inhibit XO activity in different platforms, which added further validation to the results of the virtual screening campaign.<sup>54</sup> Accordingly, a final shortened hit list of three natural products; rosmarinic acid, techtochrysin and isoferulic acid, was made available for further biological validation.

The binding mode of selected natural products representing the final hit list, as predicted by molecular docking, is shown in

Fig. 3. Initially, the visualization of the binding poses of rosmarinic acid, techtochrysin and isoferulic acid in XO crystal structure 3NVY emphasized their complete shape fitting within the water channel leading towards the Mo-pt cofactor in the XO active site (Fig. 3, lower panel). Rosmarinic acid; the top identified hit, formed five hydrogen bonds with XO key amino acid residues SER876, ARG880, THR1010, ASN768, thus hindering their involvement in catalysis (Fig. 3A and Table 3). Chemically, rosmarinic acid is composed of two fragments: caffeic acid and 3,4-dihydroxyphenyllactic acid, which are connected together *via* an ester linker. The aromatic ring of the caffeic acid moiety is sandwiched between PHE914 and PHE1009, forming strong  $\pi$ - $\pi$  stacking interactions with their side chains, in a manner similar to the binding modes observed for all substrates of the enzyme<sup>51</sup> (Fig. 3A and Table 3). Meanwhile, the free carboxylic acid group of the 3,4-dihydroxyphenyllactic acid moiety is predicted to form a salt bridge with the side chain of LYS771 under physiological conditions, thus anchoring rosmarinic acid in a pose that allows for a tight ligand-receptor interaction, and hence better blockade of xanthine substrate binding in the Mo center preventing its oxidation.

Docking studies clearly showed that the co-crystallized ligand; quercetin and other structurally analogous flavonoids; namely, luteolin, techtochrysin, kaempferol, naringenin, genkwanin, myricetin, acacetin, biochanin A, luteolin-3'-methyl-ether, quercetin-3-methylether and eriodictyol represents a cluster of good XO binders with docking scores ranging from  $-9.790$  to  $-8.660$  (Table 3). Binding mode analyses and



Table 4 Validation parameters of molecular docking for 3NVY crystalline structure

Validation parameters	3NVY
RMSD <sup>a</sup>	0.5
AUC-ROC	0.98
EF (2%)	50
EF (5%)	20
EF (10%)	10
RIE	15.15
BEDROC ( $\alpha = 8$ )	1
BEDROC ( $\alpha = 20$ )	1
BEDROC ( $\alpha = 160$ )	1
Ranked actives <sup>b</sup>	30
Approximate sensitivity	0.98
Specificity	0.99

<sup>a</sup> RMSD value was calculated for 3NVY enzyme crystalline structure with co-crystallized ligand (quercetin). <sup>b</sup> Ranked actives are the number of actives recovered from the constructed validation set.

acquired docking scores demonstrated that quercetin and related natural flavonoids bind strongly at the molybdenum center active site with their benzopyran scaffold, or at least ring A, sandwiched between the conserved phenylalanine residues; PHE914 and PHE1009, and their exocyclic carbonyl groups oriented toward ARG880 (Fig. 3B, S1 and S5,† Table 3). Meanwhile, the aromatic ring B of the investigated flavonoids was buried in the XO binding site and exerted potential hydrophobic interactions with the side chains of LEU648, PHE649, LEU873, ALA910, PHE911, PRO1076, VAL1011, PHE1013, and LEU1014 lining the enzyme hydrophobic pockets (Fig. 3B, S1 and S5,† Table 3). Except for 2,3-dihydroflavones, the flavonoids cluster interacted *via* its phenolic hydroxyl group at either C-5 or C-7 forming bidentate hydrogen bonding interactions with the side chains of both ARG880 and THR1010, thus hindering these residues from participating in catalysis (Fig. 3B, S1 and S5,† Table 3). In contrast, hesperetin and eriodictyol, with a flavonone or 2,3-dihydroflavone skeleton, maintained a single hydrogen bond through their C-7 hydroxyl group with the side chain of THR1010 only (Table 3). Meanwhile, the 2,3-dihydroflavone named naringenin hydrogen bonded with; naringenin, hydrogen bonded with the side chains of both ARG880 and THR1010, but through its C-5 hydroxyl and C-4 carbonyl groups, respectively (Table 3). Moreover, the C-4 carbonyl group of naringenin, in addition to techtochrysin and genkwanin, engages in a hydrogen bond with the backbone NH of VAL1011 (Fig. 3B and Table 3). In the case of 3-hydroxy flavones such as quercetin, kaempferol and myricetin, the C-3 hydroxyl group is attributed to a favorable hydrogen bonding interaction with GLU802 (Fig. S1,† Table 3). Collectively, these crucial interactions seemed to control the overall orientation of quercetin and are structurally related flavonoids within the Mo center conferring inhibition of XO catalysis.

Docking simulations also proposed the promising potential of some phenolic acids and phenolic esters as XO inhibitors including isoferulic acid, phenethyl-*trans*-caffeate, benzyl-*trans*-caffeate and 3-methyl-3-butenyl ferulate, with docking scores of

Table 5 *In vitro* xanthine oxidase inhibitory potential of selected *in silico* hits

Compound	IC <sub>50</sub> (μM)
Techtochrysin	0.084 <sup>f</sup> ± 0.013
Rosmarinic acid	0.97 <sup>d</sup> ± 0.042
Luteolin	1.68 <sup>c</sup> ± 0.055
Quercetin	1.98 <sup>b</sup> ± 0.062
Isoferulic acid	3.23 <sup>a</sup> ± 0.083
Febuxostat	0.02 <sup>f</sup> ± 0.003
Allopurinol	0.82 <sup>e</sup> ± 0.041
<i>F</i>	1565.403 <sup>a</sup>
<i>p</i>	<0.001 <sup>a</sup>
LSD	0.078

<sup>a</sup> Data are expressed as mean of three experiments ± SD. *F*: *F* for ANOVA test, pairwise comparison bet. Each 2 groups was done using post hoc test (LSD). *p*: *p* value for comparing between the studied groups. Means in the column with common letters are not significant (*i.e.* means with different letters are significant).

–9.557, –9.474, –9.343 and –8.616, respectively (Table 3). Detailed examination of isoferulic acid's binding pose presented the free carboxylic acid and C-6 phenolic hydroxyl groups as the main binding and anchoring pharmacophoric groups at the substrate-binding site of XO (Fig. 3C, Table 3). The free carboxylic acid group participated in a pair of important hydrogen bonds with the backbone NH of THR1010 and the side chain of ARG880 while forming a favorable salt bridge with ARG880. Meanwhile, the isoferulic acid's aromatic ring was located within the crucial hydrophobic space of the molybdopterin domain and demonstrated a strong hydrogen bond, *via* its C-6 phenolic hydroxyl group, with the side chain of SER876 (Fig. 3C, Table 3). It is interesting to note that long-chain saturated fatty acids, such as stearic and palmitic acids, maintained the same hydrogen bonds and electrostatic interactions exerted by the carboxylic acid group of isoferulic acid, whilst lacking the required bulkiness and aromaticity to fill the hydrophobic space of the Mo center, justifying their relatively weaker predicted binding affinities (Table 3).

On the other hand, phenolic esters showed a binding pattern nearly similar to that of isoferulic acid within the XO binding pocket; their methoxy and/or hydroxyl substituents at C-6 and C-7 of ring A satisfied the critical hydrogen bonding interactions with ARG880 and THR1010 (Table 3). Furthermore, a favorable  $\pi$ - $\pi$  stacking interaction was observed within 5 Å distance between aromatic ring A in phenolic esters and the side chains of PHE914 and PHE1009 (Table 3). In addition, the alcohol moiety in phenolic esters was extended to form hydrophobic interactions, *via* either its phenyl ring B in phenethyl-*trans*-caffeate (CAPA) and benzyl-*trans*-caffeate or through its aliphatic hydrocarbon chain as in the case of 3-methyl-3-butenyl ferulate, with LEU648, PRO1076, ALA1078, VAL1011, PHE1013 and LEU1014 along with the lipophilic space of XO enzyme (Table 3). Exceptionally, the aromatic ring B of CAPA was uniquely engaged in a  $\pi$ -cation interaction with the side chain of LYS771, justifying its relatively higher docking score compared with other phenolic esters (Table 3).



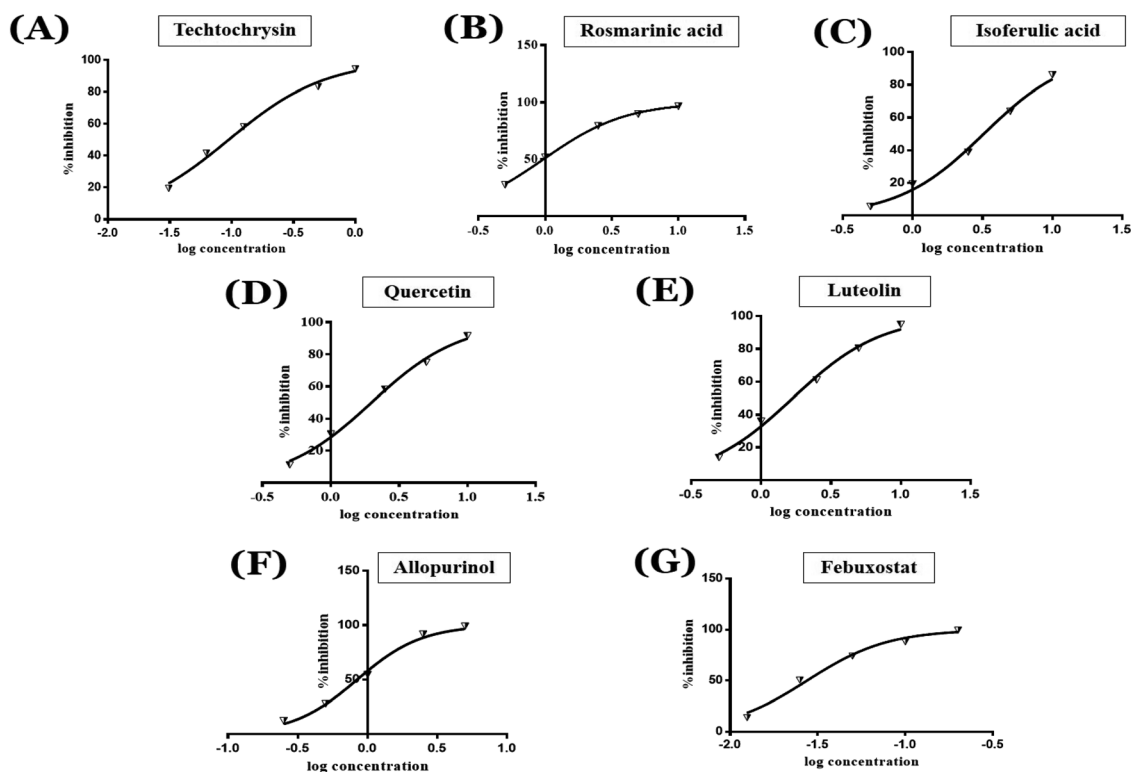


Fig. 4 Concentration-dependent inhibition of xanthine oxidase activity by the potential *in silico* hits; (A) techtchrysin, (B) rosmarinic acid, (C) isoferulic acid, (D) quercetin, (E) luteolin and two reference drugs; (F) allopurinol and (G) febuxostat, using XO spectrophotometric assay.

In summary, our computational docking simulation studies predicted the potential of certain chemical scaffolds in Egyptian propolis including phenolic acids, phenolic esters, and flavonoids as promising XO inhibitors. Binding mode analysis studies provided molecular insights into the interactions of potential *in silico* hits with the catalytically important amino acid residues at the enzyme active site. Docking results afforded a final shortened hit list of three natural products: rosmarinic acid, techtchrysin and isoferulic acid, representing different chemical classes and with supportive binding data, thus they were subjected to further biochemical evaluation.

**3.1.2. Validation of the docking process.** The docking procedure was validated using two methods; firstly, quercetin inhibitor from 3NVY was removed and re-docked into the active site to ensure the inhibitor binds exactly to the active site cleft with less deviation compared to the actual co-crystallized complex. The re-docked complex was then superimposed onto the reference co-crystallized complex with a low root mean square deviation (RMSD) of 0.5 Å (Table 4). Secondly, the so-obtained enriched validation set consisted of 30 active molecules (Table S2†) combined with 1000 decoy ligands available at the Schrödinger suite were utilized to enhance ligand enrichment, which is pivotal to assess the docking procedure and eliminate false positives. The sensitivity and specificity of Schrödinger software in predicting geometric poses and scoring protein–ligand interactions have been precisely evaluated. ROC was plotted and some predictive power indicators such as AUC-ROC, BEDROC and EF (at 2%, 5% and 10%) were calculated and detailed in Table 4.

For the sake of clarity, the ROC plot indicated that the enzyme crystal structure (3NVY) exhibited a good specificity successfully discriminating between the actives and decoys and high sensitivity detecting all the active compounds with an approximate value of 0.99 concerning the measure of how highly a randomly selected active is ranked compared to a randomly chosen decoy expressed by AUC-ROC, it was observed that 3NVY revealed an excellent value of 0.98.

As shown in Table 4, EF values revealed that the docking protocol principally retrieves active ligands out of a seeded random set, when the top 2%, 5% and 10% of the total set were considered, respectively, noting that the maximum attainable enrichment factors are 50, 20, and 10 for EF (2%), EF (5%), and EF (10%), respectively.<sup>33</sup>

To ensure optimal early recognition of actives from decoys at different tuning parameter values  $\alpha$ , BEDROC parameter was utilized recording high scores at all  $\alpha$  values. An excellent RIE value was noted highlighting the optimal performance of docking protocol in ranking active compounds at high positions of the hit list (Table 4).

### 3.2. *In vitro* xanthine oxidase inhibitory activity of the top-scoring compounds

Based on the encouraging *in silico* results, the top-scoring virtual hits were subjected to further laboratory-based *in vitro* testing with an ultimate goal of investigating new molecules to be adopted as lead compounds for the rational design of potential chemical entities with less or no side effects for the



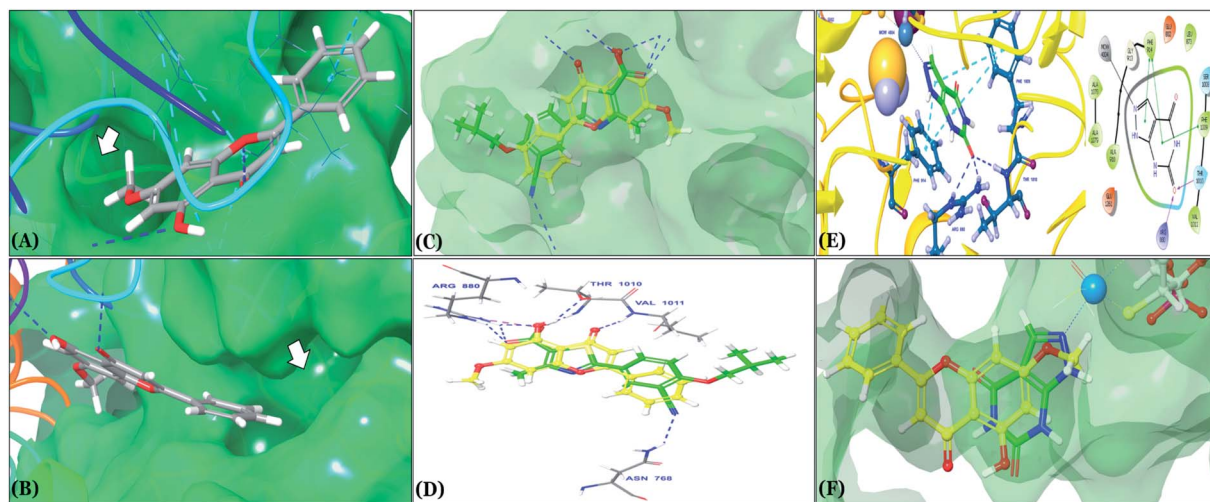


Fig. 5 (A and B) *In silico* binding pose of techtchrysin at the ATP binding site of XO crystal structure (PDB ID 3NVY). The protein surface is shown in aquamarine solid surface representation; (A) the lipophilic pocket of XO protein is indicated by an arrow, (B) the deep end of the XO binding site is indicated by an arrow (C) structure overlay for techtchrysin with the febusostat conformations (D) overlaid docked poses of techtchrysin and febusostat interacting with XO active site's amino acid residues (PDB ID 3NVY). (E) 3D & 2D diagrams of docked pose of oxipurinol interacting with XO active site's amino acid residues. (F) Structure overlay for techtchrysin with oxipurinol conformations.

treatment of hyperuricemia and associated inflammatory disease states. In this study, the *in vitro* XO inhibitory potency of the final shortened hit list including rosmarinic acid, techtchrysin and isoferulic acid, was assessed using a cell-free spectrophotometric assay by measuring uric acid levels at 295 nm. Generally, cell-free biochemical assays are widely used for XO inhibitors mining due to their automation-friendly, easy to use, relatively low cost, and wide availability. Quercetin and luteolin, with the previously reported XO inhibitory potential,<sup>54</sup> were included in the study for activity comparison and structure–activity relationship (SAR) studies. Meanwhile, allopurinol and febusostat were used as positive standard controls and their  $IC_{50}$  values were determined. Table 5 shows the concentration that resulted in 50% XO inhibition ( $IC_{50}$  values) for all tested compounds, as determined using nonlinear fitting of concentration–response data (Fig. 4). The calculated  $IC_{50}$  values of febusostat and allopurinol in this assay were 0.02 and 0.82  $\mu\text{M}$ , respectively, which were consistent with their reported values,<sup>11,52</sup> validating the results of this study.

As shown in Fig. 4, the results of the XO assay demonstrated the ability of all investigated compounds to significantly inhibit the formation of uric acid catalyzed by XO in a dose-dependent manner, which in turn validated the results of the virtual study. Among the tested compounds, techtchrysin was found to possess the greatest potency; with an  $IC_{50}$  value in the nanomolar range ( $IC_{50} = 0.084 \mu\text{M} \pm 0.013$ ). The XO inhibitory activities of other tested hits decreased in the order of rosmarinic acid ( $IC_{50} = 0.97 \mu\text{M} \pm 0.042$ ), luteolin ( $IC_{50} = 1.68 \mu\text{M} \pm 0.055$ ), quercetin ( $IC_{50} = 1.98 \mu\text{M} \pm 0.062$ ) and isoferulic acid ( $IC_{50} = 3.23 \mu\text{M} \pm 0.083$ ) (Table 5).

Earlier studies highlighted the structure–function relationship of flavonoids interacting with XO enzyme and revealed some key structural features in the flavonoids class proved to be important in terms of effective XO inhibition; (i) the conjugated

2-phenyl benzopyran scaffold seemed desirable and complemented the shape of the active site, (ii) the exocyclic carbonyl group at position 4 appeared to be essential for effective inhibition, and (iii) the presence of hydroxyl groups at positions 5 and 7 of ring A was likely crucial for XO inhibitory activity and contributed significantly to the binding affinity.<sup>4</sup>

Structure–activity relationship studies (SARs) for the tested flavonoids in this study have been summarized in Fig. 6C. As shown in Table 3, the three tested flavonoids shared a central planer skeleton including a conjugated three-ring backbone, a hydroxy group at position 5 and an oxygenated aromatic carbon at position 7. However, techtchrysin displayed a much lower  $IC_{50}$  value and hence significantly higher potency, when compared with luteolin and quercetin as XO inhibitors (Table 5). The variability among studied flavonoids was due to different substitution patterns at positions 7 of the A ring and 3', 4', 5' of the B ring as well as position 3 of the C ring (Table 3). Despite the fact that both quercetin and luteolin possessed hydroxyl groups at C-5 and C-7 of ring A, they exhibited a weaker XO inhibitory profile when compared with techtchrysin (Table 5). Interestingly, the replacement of one hydroxyl group at position 7 with a methoxy substituent in techtchrysin, while maintaining the second hydroxyl at C-5, resulted in a dramatically more active derivative, consistent with a previous report.<sup>55</sup> Docking studies further justified this activity enhancement; the techtchrysin's C-7 methoxy group, despite lacking hydrogen bonding interactions, occupied lipophilic pocket-forming favorable hydrophobic interactions with the side chains of PHE914, PHE1005, ALA1078 and ALA1079 along with the lipophilic space of XO enzyme (Fig. 3B and 5A, Table 3). These hydrophobic interactions might explain, at least in part, the significant impact of the C-7 methoxy group on activity improvement in techtchrysin, compared with related flavonoids possessing hydroxyl group at this position, and





underscore the importance of only one hydroxyl group in ring A for flavonoids binding and subsequent XO inhibitory capacity (Table 5). Typically, the C-7 methoxy group resided between PHE914 and the residue at the tip of the lipophilic pocket, PHE1005; nevertheless, it was not sufficiently bulky enough to perfectly fill the pocket or lacked the aromaticity to engage in  $\pi$ -electron interactions with the aromatic residues shaping the pocket (Fig. 3B and 5A). Therefore, increasing the bulkiness at this site is expected to enhance the XO binding affinity and subsequent inhibitory potency. Additional studies should be conducted to identify the substituent with optimal size at the C-7 position of teichochrysin. Despite its participation in a hydrogen bond with GLU802 in our docking studies, the results of the enzymatic assay showed that the presence of a hydroxyl group at position 3 of the flavonoids C ring negatively influenced the XO inhibitory activity, as evidenced by the weaker suppression ability of the 3-hydroxyl substituted benzopyran of quercetin *versus* the C-3 unsubstituted luteolin (Tables 3 and 5, Fig. S1, S5<sup>†</sup>). It is also important to point out that the  $IC_{50}$  values of quercetin and luteolin in this assay were consistent with their reported values, adding further validation for the results of this study.<sup>50,54</sup>

As expected from our binding mode studies, teichochrysin's ring B is important to enable the molecular extension and access the deep end of the XO binding site demarcated by LEU648, PHE649, LEU873, ALA910 and PHE911 (Fig. 3B and 5B, Table 5). However, the presence of hydroxyl groups at C-3' and

C-4' of ring B in luteolin and quercetin were presumed to be another reason underlying the tremendous difference in their XO inhibitory activities from teichochrysin (Table 5). This could be attributed to the fact that the pocket where ring B resided is entirely hydrophobic; hence the two hydroxyls exhibited multiple unfavorable van der Waal interactions with LEU648, PHE649, LEU873, VAL1011 and PHE1013 leading to a serious energy penalty and thus, negatively influencing the activity (Fig. S6<sup>†</sup>). Furthermore, a previous report has demonstrated the negative impact of the C-4'-hydroxyl group on the potency of flavonoid-based XO inhibitors, corroborating the results of this study.<sup>1</sup>

In an attempt to better understand whether positions 3' and 4' of teichochrysin's B ring are amenable for future optimization, structural overlay studies were conducted for teichochrysin with the antigout drug; febuxostat, at the XO binding site of the crystal structure 3NVY (Fig. 5C and D). It is noteworthy that febuxostat was 4 fold more active than teichochrysin in the XO cell-free assay, justifying its selection for overlay studies (Table 5). The space occupied by teichochrysin was similar to that exploited by febuxostat, where the teichochrysin's benzopyran core perfectly superimposed with the substituted thiazole moiety of febuxostat, which in turn formed multiple non-covalent salt bridges, hydrogen bonds and  $\pi$ - $\pi$  stacking interactions with the catalytic amino acid residues; ARG 880, THR1010, PHE914 and PHE1009 (Fig. 5D and S2, <sup>†</sup> Table 3). It is worth noting that the fitting of teichochrysin and febuxostat to

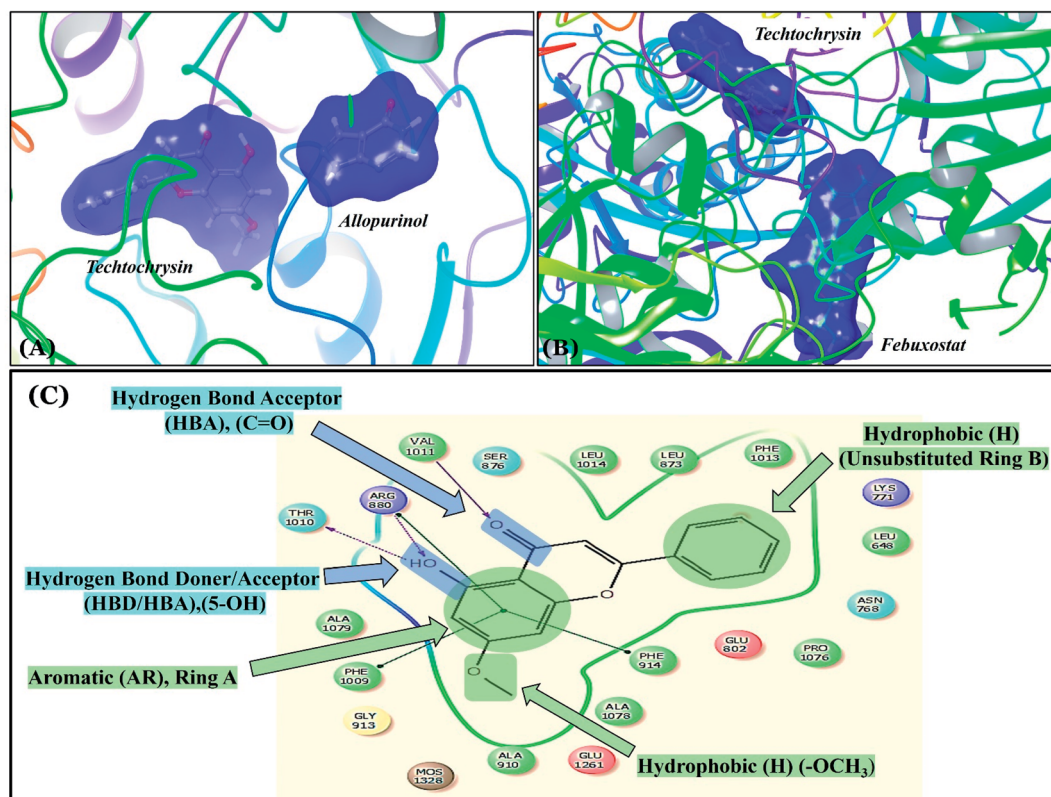


Fig. 6 (A) Sequential docking of allopurinol and teichochrysin at the XO binding site (PDB ID 3NVY). (B) Sequential docking of febuxostat and teichochrysin at the XO active site. (C) 2D teichochrysin/XO active site's amino acid residues interactions diagram summarizing the observed structure-activity relationship studies (SARs) of teichochrysin (*i.e.* flavonoid class) for effective XO inhibition.



the enzyme's active site was consolidated by free rotation of the region connecting their aforementioned overlaid cores with an aromatic ring. Therefore, the two inhibitors efficiently matched the structure of the substrate entering channel leading towards the Mo-pt cofactor in the XO active pocket, adding further justification to the results of the enzymatic assay (Fig. 5C, Table 5).

Interestingly, the aromatic ring A of febuxostat almost overlaid the unsubstituted teicho-chrysin's B ring, however, the nitrile group at its 3-position whilst retaining the hydrophobic character extended to form a strong hydrogen bond with the side-chain amide of ASN768 (Fig. 5D and S2,† Table 3). Although this asparagine residue is located away from the active center for direct participation in substrate recognition or catalytic activity, the nitrile group of febuxostat was essential for potent XO inhibitory activity.<sup>56</sup> Meanwhile, a bulky hydrophobic isobutoxy group at position 4 efficiently filled the remaining available lipophilic space within the channel and was also crucial for tight XO binding.<sup>56</sup> This could explain the relatively higher potency of febuxostat *versus* teicho-chrysin in the cell-free assay (Table 5). Furthermore, these observations implied that the unsubstituted pattern at C-3' and C-4' of teicho-chrysin is not sufficient for optimal XO inhibition and characterized ring B's key pharmacophores likely to impart higher binding affinity towards XO that would be of great importance in guiding the future optimization of teicho-chrysin as a potential XO inhibitor. Firstly, increasing the bulkiness at the unsubstituted C-3'-position of teicho-chrysin by adding an isobutoxy group, mimicking the overlaid C-4 in febuxostat's ring A, should improve its XO binding affinity (Fig. 5C). However, the situation regarding the teicho-chrysin's C-4' is quite dissimilar; it adopted a slightly different conformation compared with the nitrile-substituted C-3 in febuxostat's ring A (Fig. 5C). Due to its linear geometry, the nitrile substituent projected into a narrow hydrophobic subpocket/cleft and formed a hydrogen bond in a sterically congested environment (Fig. 5C and D). Despite the imperfect overlay between C-3 and C-4' of febuxostat and teicho-chrysin, respectively, introducing a nitrile group at teicho-chrysin's C-4' would still be a valid strategy to enhance the XO binding affinity due to the dynamic flexibility of active site.<sup>57</sup> To mimic this, a second possible direction for future optimization of teicho-chrysin as a novel XO inhibitor can be implemented by introducing a small hydrophobic angular substituent, such as methoxy group, at C-4' to efficiently fill the XO hydrophobic subpocket, where the nitrile group resides, whilst retaining the hydrogen bond acceptor property to engage in a hydrogen bond with ASN768. The small lipophilic subpocket could still be able to accommodate this methoxy group with a small conformational shift due to the plasticity of the protein in molding the Mo-pt center to the shape of the ligand in the binding site,<sup>58</sup> and yet the XO inhibitory effect might be improved by fine-tuning modifications at 4'-position. Future optimization in the aforementioned directions is predicted to improve the teicho-chrysin's binding affinity, drug-likeness, and its subsequent XO inhibitory potential.

Compared with the well-reputed XO inhibitor; allopurinol, teicho-chrysin demonstrated 10-folds enhancement in the XO

inhibitory activity in the implemented enzymatic assay (Table 5, Fig. 4). It is important to highlight that allopurinol is a potent suicide XO inhibitor; it will be further hydroxylated by the enzyme to provide the actual potent XO inhibitor namely, oxipurinol.<sup>59</sup> Therefore, oxipurinol has been docked into the XO protein (PDB ID 3NVY, Fig. 5E) and overlaid with teicho-chrysin within the binding site (Fig. 5F). As expected, oxipurinol coordinated directly and bound tightly to the reduced molybdenum ion of the enzyme (Mo(IV)). In contrast, teicho-chrysin fitted well into the substrate-binding channel of the enzyme whilst not forming any interaction with the molybdenum metal atom. Therefore, it has been proposed that teicho-chrysin and allopurinol have different binding modes that are, structure-based and mechanism-based, respectively. In other words, teicho-chrysin could hinder the approach of the substrate toward Mop-terin domain and eventually prevent its oxidation to uric acid. Importantly, this overlay study implied a kind of cooperativity between teicho-chrysin and allopurinol in modulating the catalytic activity of XO if used together and opened a new direction to assess this hypothesis virtually through sequential docking of the two inhibitors (Fig. 6A). Interestingly, allopurinol and teicho-chrysin maintained their binding poses and fitted cooperatively within the binding site of XO, which may suggest both structure- and mechanism-based inhibition of catalysis if both compounds were used in combination settings. The proposed hypothesis was also tested for febuxostat along with teicho-chrysin (Fig. 6B). Due to the plasticity of the protein, the two compounds were able to amazingly fit within the XO active site and nearly no open space was left in the channel after their binding. Such promising virtual cooperativity provided substantive guidance to further evaluate this hypothesis through MD simulation studies (Section 3.3) and in biochemical settings using combination analysis studies (Section 3.4).

The present study intuitively demonstrated that the two tested phenolic acids rosmarinic acid and isoferulic acid significantly suppressed the formation of uric acid catalyzed by XO in a dose-dependent manner. Their IC<sub>50</sub> values indicated that rosmarinic acid possessed a strong inhibitory activity (IC<sub>50</sub> = 0.97 ± 0.042 μM) on XO than isoferulic acid (IC<sub>50</sub> = 3.23 ± 0.083 μM). This obvious potency difference might be attributed to the number of free hydroxyl moieties on the benzene rings<sup>60</sup> as shown in their chemical structures (Table 3). SARs for the tested phenolic acids in this study have been summarized in Fig. S7.† Rosmarinic acid bears four hydroxyl groups on the benzene rings that appeared to promote the XO inhibitory activity *via* the formation of multiple hydrogen bond interactions with active site residues of the enzyme and subsequently hindered substrate linkage in (Mo-pt) active site, while isoferulic acid carries only one hydroxyl group. Even though rosmarinic acid exhibited high IC<sub>50</sub> relative to febuxostat (IC<sub>50</sub> = 0.02 ± 0.003) yet its inhibitory activity was comparable to that of allopurinol (IC<sub>50</sub> = 0.82 ± 0.041) as presented in (Table 5).

Collectively, the *in silico* binding studies presented herein offered an efficient basis for the structure-based design of novel XO inhibitors. These results could be an inspiration for further investigation of potential XO inhibitors derived from Egyptian propolis. From the above experimental findings together with *in*



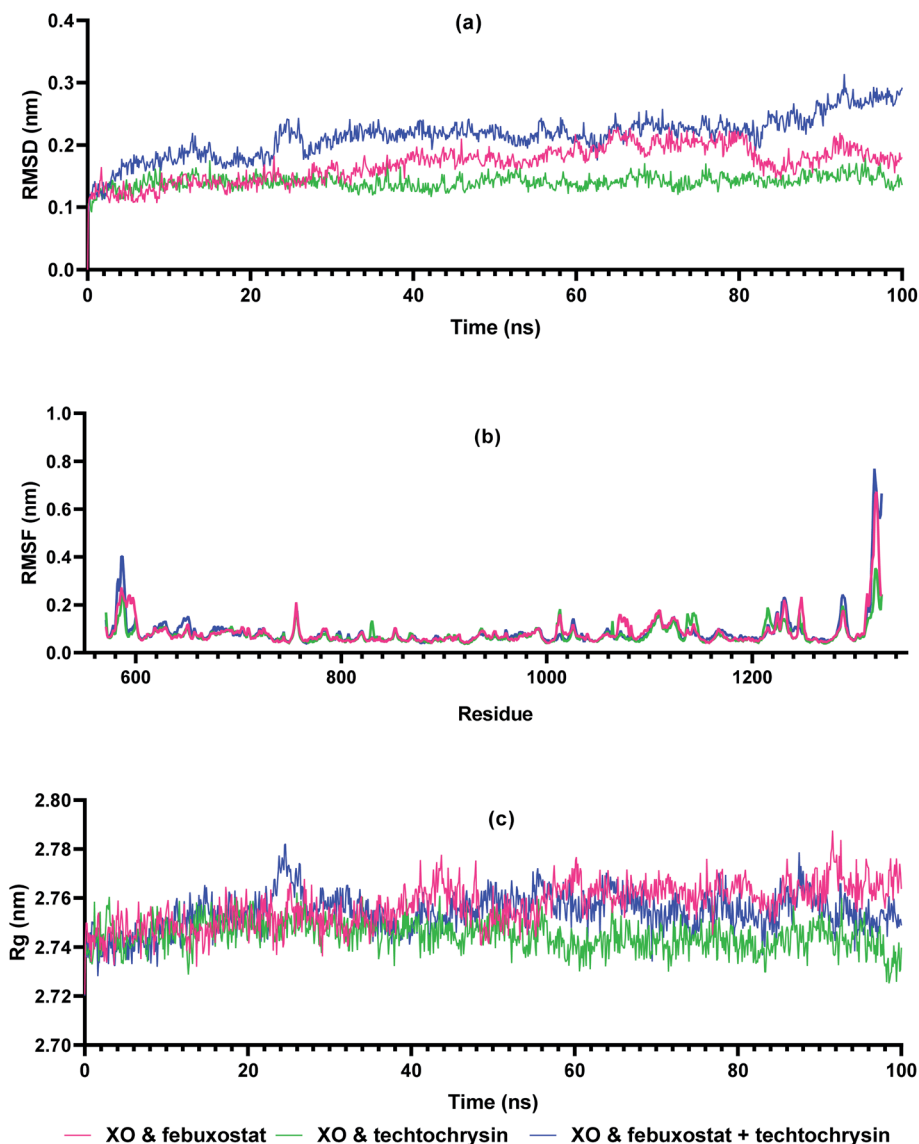


Fig. 7 Trajectory analysis of molecular dynamics simulation of enzyme–ligand complexes of xanthine oxidase (XO) enzyme with reference compound febuxostat, active hit techtchrysin, and combination of febuxostat and techtchrysin. (a) RMSD values of XO–febuxostat (red), XO–techtchrysin (green) and XO–febuxostat + techtchrysin (blue) complexes, (b) RMS fluctuation, and (c)  $R_g$  measurement over 100 ns.

*in silico* results, we suggested that both techtchrysin and rosmarinic acid could be adopted as potential hits for the development of novel naturally derived therapeutics for the treatment of hyperuricemia. However, further studies are needed to claim these candidates for clinical investigation.

### 3.3. Molecular dynamics simulations

Molecular dynamics simulations are very useful in drug discovery phases to predict the stability of protein–ligand complexes in the *in silico* physiological environment.<sup>64</sup> In this study, the stability of febuxostat, techtchrysin, and their combination with XO was investigated using MD simulation. Input files for MD simulation of enzyme–ligand complexes obtained from Glide XP were created using amber FF19SB *via* CHARMM-GUI FF-Converter. MD simulation of 100 ns duration was performed for each complex. Trajectory RMSD, RMSF, and

$R_g$  analyses were made and binding free energy calculations were acquired.

The RMSD measurement in MD simulations is the main parameter that provides information about protein stability and deviation.<sup>62</sup> The stability of the RMSD graph after the pre-stage MD simulation indicates that the system is stabilizing. As shown in Fig. 7a, XO–febuxostat, XO–techtchrysin, and XO–febuxostat + techtchrysin complexes remained below 0.3 nm, and mean RMSD values of 0.16 nm, 0.14 nm, and 0.21 nm were measured for the three investigated complexes, respectively. RMSF measurements are another parameter that provides information about protein fluctuation and conformational changes.<sup>63</sup> As seen in Fig. 7b, RMSF values fluctuated below 0.3 nm for all three complexes except for the N- and C-terminals of XO. Another parameter,  $R_g$ , provides information on protein–ligand compactness.<sup>64</sup> A low and stable  $R_g$  value indicates the



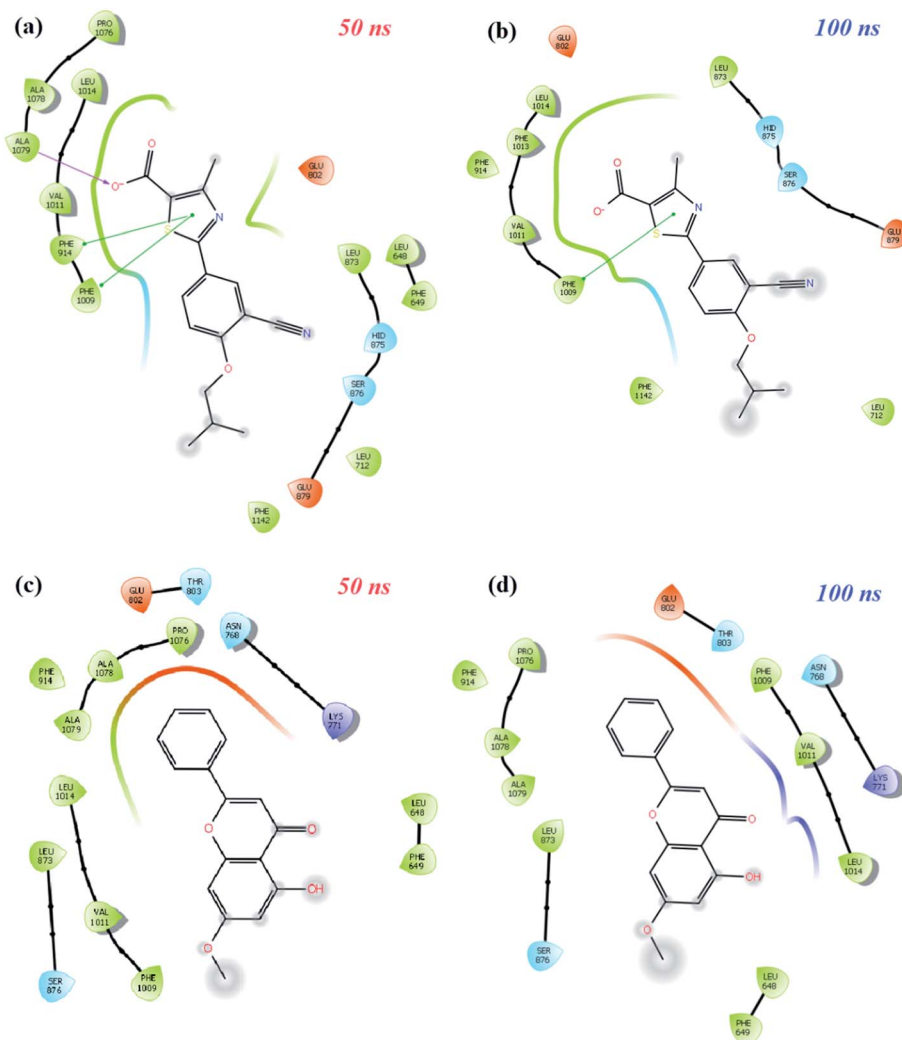


Fig. 8 Diagrams of protein–ligand interactions of XO-febuxostat and XO-techtchrysin complexes at the middle and end of 100 ns time simulations. (a and b) Schematic protein–ligand interaction 2D diagrams of the XO-febuxostat complex at (a) 50 ns, (b) 100 ns of MD simulations. (c and d) Schematic protein–ligand interaction 2D diagrams of XO-techtchrysin complex at (c) 50 ns, (d) 100 ns of MD simulations.

stability of the protein–ligand complex. As shown in Fig. 7c, XO-febuxostat, XO-techtchrysin, and XO-febuxostat + techtchrysin complexes remained stable between 2.74 and 2.78 nm, measuring 2.76 nm, 2.74 nm, and 2.75 nm on average for the three complexes, respectively.

MD simulation animations of 100 snapshots between 0 and 100 ns were created as provided in ESI 3<sup>†</sup> to analyze and compare the stability of XO-febuxostat, XO-techtchrysin, and XO-febuxostat + techtchrysin protein–ligand complexes. In addition, XO-febuxostat and XO-techtchrysin protein–ligand interactions at 50 and 100 ns are shown in Fig. 8, while XO & febuxostat + techtchrysin protein–ligand interactions are provided in Fig. 9.

As shown in Fig. 8a and b, the pi–pi stacking interaction with the 50 and 100 ns PHE1009 of XO-febuxostat complex MD simulation was preserved and remained stable. As shown in Fig. S8a,<sup>†</sup> the RMSD value for the XO-febuxostat complex was measured below 0.20 nm with an average of 0.091 nm during the 100 ns MD simulation of febuxostat. Meanwhile, as shown

in Fig. 8c and d, the hydrophobic interactions with PHE1009, VAL1011, LEU1014, ASN768, and LYS711 have been maintained in the XO-techtchrysin complex, while the ligand remained stable as well. Interestingly, the RMSD value of techtchrysin was calculated in the XO-techtchrysin complex to be below 0.08 nm with a mean of 0.056 nm, implying a more stable system when compared with the XO-febuxostat complex, highlighting the potential of techtchrysin as a promising hit (Fig. S8b<sup>†</sup>).

Finally, protein–ligand interactions in the XO-febuxostat + techtchrysin complex were analyzed. As shown in Fig. 9a and b, the techtchrysin's pi–cation interaction with ARG912 and hydrophobic interaction with PHE798 remained stable. In addition, the hydrophobic interactions exerted by febuxostat with LEU648, LYS771, VAL1011, PHE1013, and LUE1014 have been preserved (Fig. 9c and d). As shown in Fig. S8c,<sup>†</sup> RMSD values of techtchrysin and febuxostat in the XO-febuxostat + techtchrysin complex were calculated as an average of 0.047 nm and 0.099 nm, respectively.



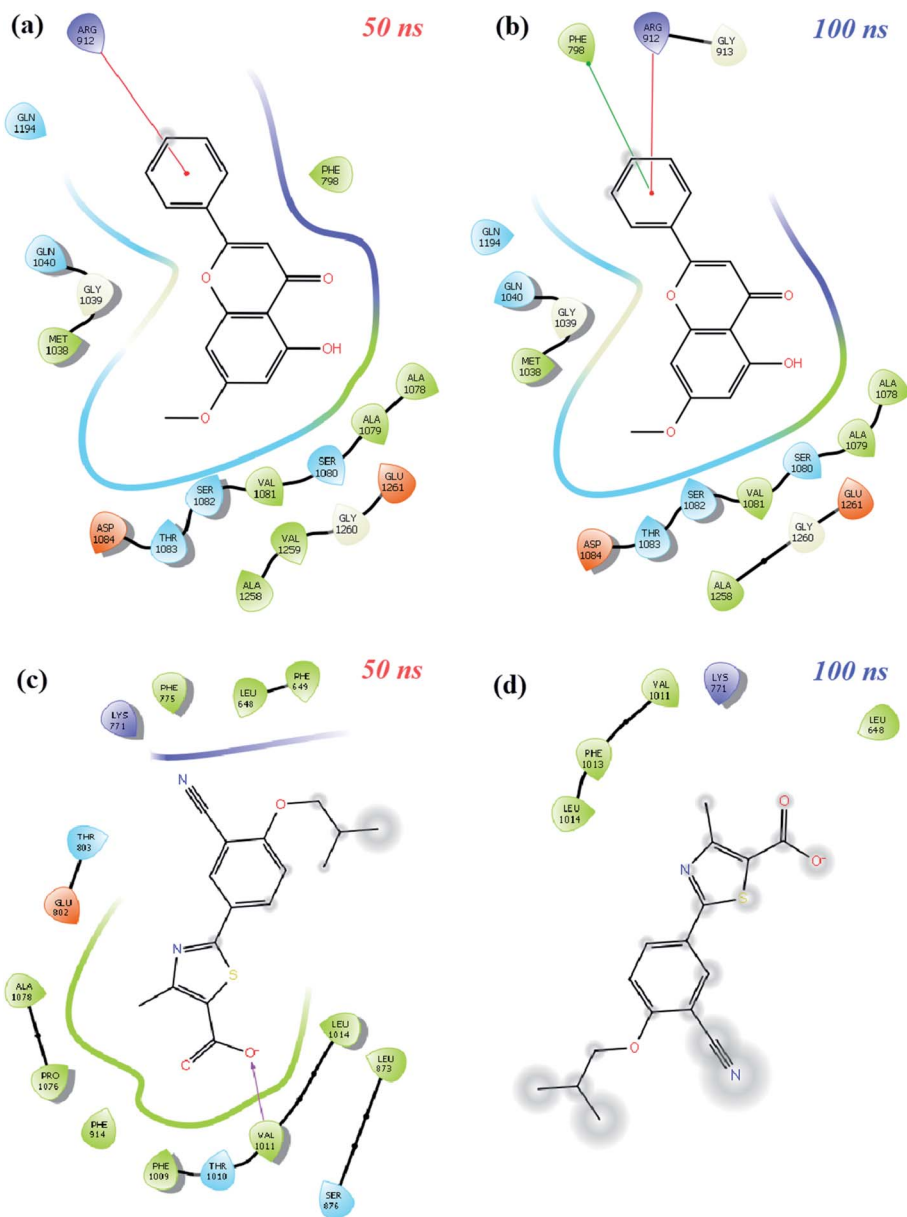


Fig. 9 Schematic protein–ligand 2D interactions of (a and b) techtchrysin (0.47) and (c and d) febuxostat (0.99) at 50 ns and 100 ns in the XO-febuxostat + techtchrysin enzyme ligand complex.

Table 6 MM-PBSA binding free energies of XO with febuxostat, techtchrysin and combination of febuxostat and techtchrysin between 60 ns and 80 ns

Parameters Energy (kJ mol <sup>-1</sup> )	Enzyme–ligand complexes		
	XO febuxostat	XO techtchrysin	XO febuxostat + techtchrysin
van der Waals	-130.579 ± 8.794	-116.160 ± 8.808	-305.083 ± 17.785
Electrostatic	-4.010 ± 5.965	-29.914 ± 7.183	-41.452 ± 12.930
Polar solvation	85.946 ± 15.337	89.942 ± 9.335	215.747 ± 15.410
SASA	-16.184 ± 0.933	-14.028 ± 0.778	-29.371 ± 1.458
<b>Binding free</b>	<b>-64.827 ± 12.697</b>	<b>-70.160 ± 10.891</b>	<b>-160.158 ± 18.514</b>

Another important feature of MD simulation studies is that they are useful to measure the binding free energy between the protein and its ligand depending on time.<sup>65</sup> Binding free energy

is usually obtained from the energy of the MM-PBSA protein–ligand complex, subtracting the total energy of the protein and ligand and the sum of the van der Waals, electrostatic, polar



**Table 7** Dose-effect curve parameters of techtochrysin and rosmarinic acid individually and their binary combinations with each of allopurinol and febuxostat<sup>a</sup>

Drug	Dose-effect curve parameters		
	$D_m$ ( $\mu\text{M}$ )	$m$	$r$
Techtochrysin	0.081	1.73	0.98
Rosmarinic acid	1.042	1.78	0.99
Allopurinol	0.88	1.44	0.98
Febuxostat	0.022	1.57	0.99
Techtochrysin + allopurinol	0.89	1.21	0.98
Techtochrysin + febuxostat	0.032	1.12	0.99
Rosmarinic acid + allopurinol	0.93	1.42	0.98
Rosmarinic acid + febuxostat	0.45	1.13	0.98

<sup>a</sup> The parameters  $D_m$ ,  $m$  and  $r$  are the antilog of  $x$ -intercept, the slope and the linear correlation coefficient of the median-effect plot, respectively which signifies the shape of the dose-effect curve. CompuSyn software was used for automated calculations.

solvation, and SASA energies. In this study, MM-PBSA measurements of XO-febuxostat, XO-techtochrysin, and XO-febuxostat + techtochrysin complexes were performed using frames between 60 ns and 80 ns, taking into account the fluctuations in the RMSD graph. As shown in Table 6, the binding free energies of XO-febuxostat, XO-techtochrysin and XO-

febuxostat + techtochrysin complexes were measured as  $-64.827 \pm 12.697 \text{ kJ mol}^{-1}$ ,  $-70.160 \pm 10.891 \text{ kJ mol}^{-1}$  and  $-160.158 \pm 18.514 \text{ kJ mol}^{-1}$ , respectively. Accordingly, techtochrysin has a higher MM-PBSA value than febuxostat, and the combined use of febuxostat + techtochrysin has higher binding free energy than the sum of the febuxostat and techtochrysin complexes separately. It is interesting to note that the results of MD simulation studies corroborated the techtochrysin/febuxostat cooperative binding hypothesis and clearly demonstrated that the combined use of techtochrysin and febuxostat could bind to XO more potently than either febuxostat or techtochrysin alone conferring an increased stabilization of the system.

### 3.4. Study of synergistic inhibitory activity on XO

Computational approaches and screening technologies have evolved substantially over time and facilitated analysis of experimental combination data to evaluate the nature and extent of drug-drug interaction, *i.e.*, synergistic, additive or antagonistic.<sup>43</sup> Owing to the distinct XO inhibitory activity of Egyptian propolis-derived constituents; techtochrysin and rosmarinic acid, they were forwarded to combination analysis with each of allopurinol and febuxostat aimed at exploiting natural products more effectively in combination therapy to minimize

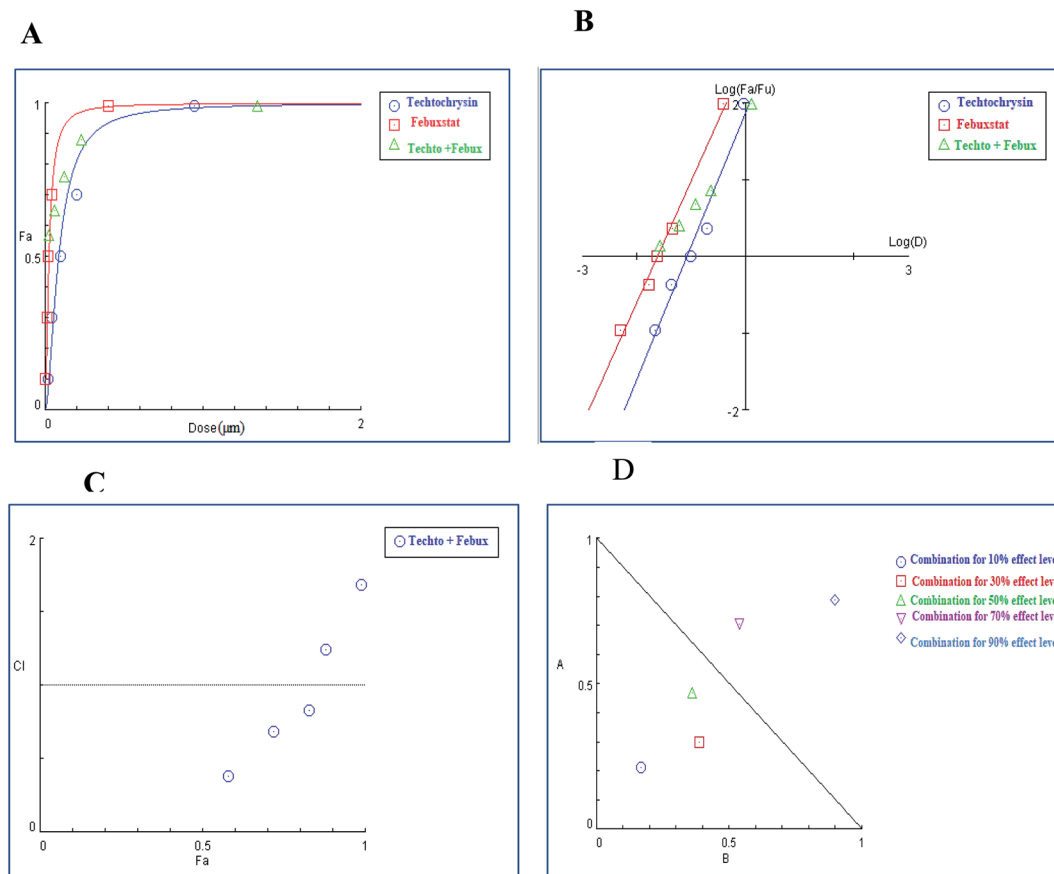


**Fig. 10** Combination analysis of techtochrysin and febuxostat (A) dose-effect curve and its linearization with the (B) median-effect plot for a single and combination treatment (C) combination index plot. (D) Dose-normalized isobologram for several effects (10%, 30%, 50%, 70 and 90%) in the combinations of techtochrysin and febuxostat.



**Table 8** Fractional inhibition of XO, combination index (CI) values and DRI values of techtochrysin and febuxostat in combination dose at different effect levels<sup>a</sup>

(Fa × 100)% (XO) inhibition of the combined drugs	CI values	Dose (μM) techtochrysin	Dose (μM) febuxostat	DRI techtochrysin	DRI febuxostat
53%	0.39 (Syn)	0.11	0.027	4.82	5.40
69%	0.61 (Syn)	0.20	0.044	4.54	2.59
75%	0.76 (Syn)	0.25	0.054	3.06	2.27
84%	1.26 (Ant)	0.39	0.081	1.42	1.77
94%	1.58 (Ant)	0.96	0.17	1.09	1.49

<sup>a</sup> CI < 0.9, (0.9–1.1), and >1.1 indicate synergism (Syn), additive effect (Add), and antagonism (Ant), respectively. Fa signifies fraction affected. DRI > 1 indicates favourable dose reduction (in fold) for the drug in combination.

the untoward side-effects of synthetic drugs while retaining the therapeutic efficacy as well as searching for the best synergistic drug combinations. For this purpose, we evaluated the nature of techtochrysin and rosmarinic acid interactions each with both febuxostat and allopurinol against XO.

**3.4.1. The median-effect analysis approach for evaluating combined drug interactions.** Based on Chou's theory derived from the median-effect principle,<sup>43</sup> a specific dose-effect curve representing the following parameters ( $D_m$ ,  $m$  and  $r$ ) of all inhibitors singly and in binary combinations were created. The  $D_m$  and  $m$  could be automatically determined from the median-effect equation (eqn (2)) by using CompuSyn software or even by using a pocket calculator.

In the median-effect plot,  $D_m$  (analogous to the  $EC_{50}$ ) represented the half-maximum effective concentration required to produce 50% enzymatic activity reduction and could be calculated as the antilog of the  $x$ -intercept as illustrated in (eqn (2')),  $m$  is the slope and  $r$ -value is the linear regression correlation coefficient of the median-effect plot.

As shown in Table 7,  $D_m$  values for techtochrysin and rosmarinic acid when combined with febuxostat were lower than the expected additive effect of each individual agent indicating a moderate degree of synergy at a 50% effect level. Whereas allopurinol displayed  $D_m$  values for combinations approached the average sum of each individual agent effect, indicating additive effect at 50% effect level.

In brief,  $D_m$  values for a single entity and their binary combinations were served as a universal reference point used for predicting synergism or antagonism at different effect levels based on CI eqn (3) and generating combination index (CI) plot.<sup>45</sup> ( $r$ -value) was >0.97 in all cases, indicating the conformity of the data to the median-effect principle (Table 7).

**3.4.2. Isobolographic, combination index (CI) and dose reduction index (DRI) analyses for evaluating drug–drug interaction.** In addition to molecular and pharmacological characteristics of drugs, there are undoubtedly other factors underlying the effectiveness of drug combinations such as drug ratios, drug concentrations and desired potency. With our aim of investigating the pharmacological relationships between techtochrysin and rosmarinic acid with both allopurinol and febuxostat in order to rationally develop efficacious combination therapeutics that might significantly improve patient outcomes in gout, multiple rigorous methods concerning with

the study of combination effects such as isobolographic, combination index, dose reduction index (DRI) analyses were extensively applied for revealing the kind and extent of drug interactions. It was noted that these methods offered complementary information and yielded similar conclusions.

**3.4.2.1. Combination analysis of techtochrysin with each febuxostat and allopurinol.** The combination of techtochrysin with either allopurinol or febuxostat significantly diminished the enzymatic activity compared to single component treatment. Over the full range of drug effect levels, the techtochrysin and febuxostat interactions were universally synergistic at lower effect levels.

In the binary combination of techtochrysin and febuxostat, the combination data points at 10%, 30% and 50% effect levels were on the synergy side (CI < 1) (Fig. 10C) indicating that the XO inhibition was markedly enhanced when techtochrysin was combined with febuxostat at low doses as summarized in Table 8.

Isobolographic analysis, which graphically represented changes in the extent of interaction as a function of techtochrysin and febuxostat concentrations confirmed that at an effect level lower than 70% inhibition, the combination data points were located below the line of additivity indicating synergism (Fig. 10D). Whereas, at 70% and 90% effect level, the combination data points set above the additivity line of indicating that techtochrysin and febuxostat in higher doses produced a lower effect in combination than the expected from additivity and could be directly interpreted as antagonism (Fig. 10D).

Furthermore, our dose reduction index (DRI) analysis (Table 8) demonstrated that a decline of enzymatic activity by 53%, required 0.11 μM techtochrysin or 0.027 μM febuxostat. However, a combination of techtochrysin and febuxostat diminished their concentrations by 4.82 and 5.40-folds, respectively, (*i.e.* 0.024 μM techtochrysin + 0.005 μM febuxostat) to achieve the same enzymatic activity reduction. These findings clearly recommend the combination of techtochrysin and febuxostat as excellent candidates for further clinical studies as they provided better therapeutic effect with better safety profile due to the lower dose needed from each individual agent in the combination treatment.

In contrast to the remarkable synergistic effect of lower dose levels of both techtochrysin and febuxostat on XO inhibition,



**Table 9** Fractional inhibition of XO, combination index (CI) values and DRI values of techtochrysin and allopurinol in combination dose at different effect levels<sup>a</sup>

(Fa × 100)% (XO) inhibition of the combined drugs	CI values	Dose (μM) techtochrysin	Dose (μM) allopurinol	DRI techtochrysin	DRI allopurinol
19%	1.69 (Ant)	0.031	0.29	1.32	1.06
35%	1.48 (Ant)	0.064	0.54	1.39	1.29
57%	1.28 (Ant)	0.15	1.13	1.78	1.38
91%	0.69 (Syn)	0.98	5.76	3.51	2.36
97%	0.53 (Syn)	3.19	15.91	3.63	3.92

<sup>a</sup> CI < 0.9, (0.9–1.1), and >1.1 indicate synergism (Syn), additive effect (Add), and antagonism (Ant), respectively. Fa signifies fraction affected. DRI > 1 indicates favourable dose reduction (in fold) for the combination.

maximal synergy could be seen from higher dose levels of techtochrysin-allopurinol combination treatment, which produced a higher magnitude of enzymatic activity reduction (Table 9). At 70% and 90% effect levels, the combination data points were below the diagonal line of additivity in dose-normalized isobologram (Fig. 11D) with CI 0.69 and 0.53, respectively, as shown in Table 9. Additionally, the dose

requirements for allopurinol decreased by 2.36-fold to achieve 70% XO inhibition as a read-out for synergy. This reduction in drug dose level, also referred to as the dose reduction index (DRI), was markedly obvious at the 90% effect level at which the allopurinol dose was reduced up to 3.92-fold (Table 9).

3.4.2.2. *Combination analysis of rosmarinic acid with each of febuxostat and allopurinol.* Meanwhile, the results shown in

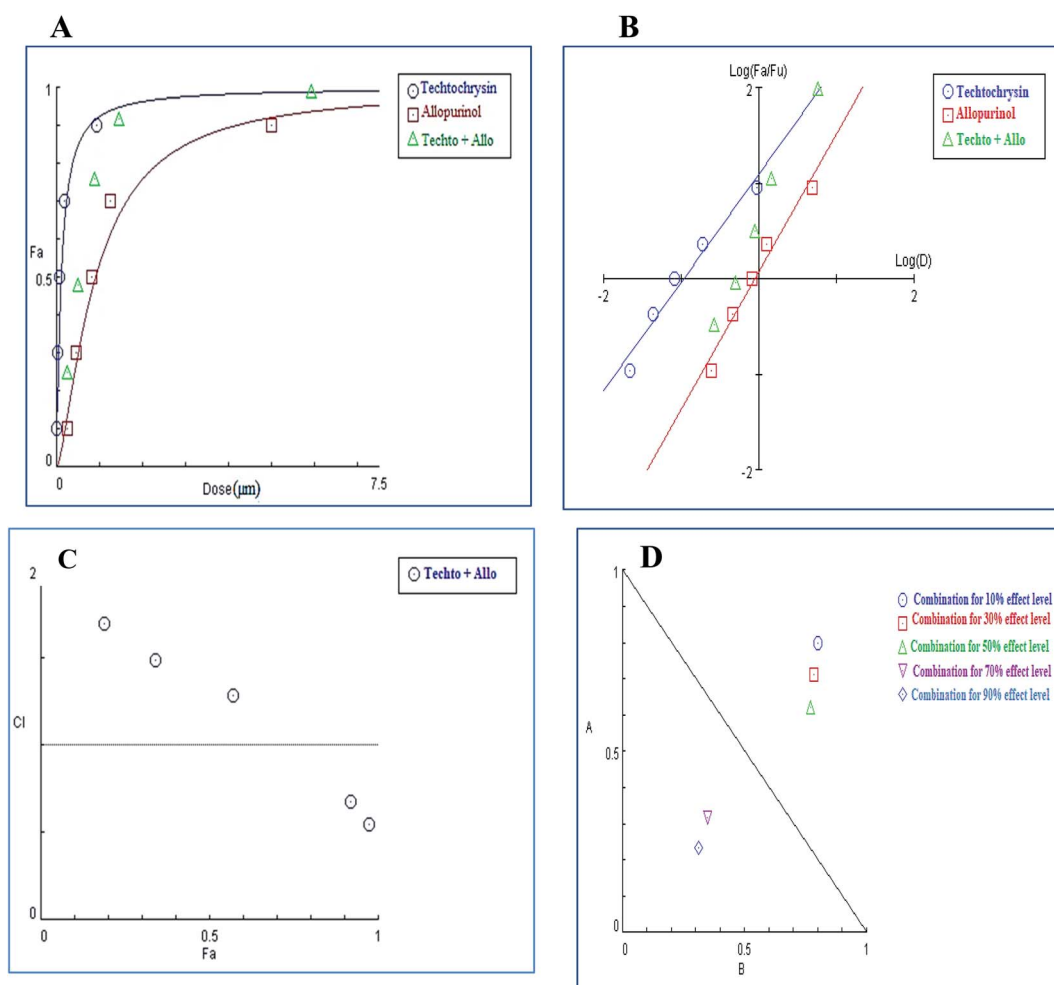


**Fig. 11** Combination analysis of techtochrysin and allopurinol; (A) dose-effect curve and its linearization with the (B) median-effect plot for a single and combination treatment (C) combination index plot. (D) Dose-normalized isobologram for several effects (10%, 30%, 50%, 70 and 90%) in the combinations of techtochrysin and allopurinol.





**Table 10** Fractional inhibition of XO, combination index (CI) values and DRI values of rosmarinic acid and febuxostat in combination dose at different effect levels<sup>a</sup>

(Fa × 100)% (XO) inhibition of the combined drugs	CI values	Dose (μM) rosmarinic acid	Dose (μM) febuxostat	DRI rosmarinic acid	DRI febuxostat
42%	0.56 (Syn)	0.87	0.02	3.13	4.04
66%	0.68 (Syn)	1.78	0.041	3.72	2.42
74%	0.85 (Syn)	2.35	0.054	2.42	2.25
82%	1.31 (Ant)	3.42	0.078	1.46	1.70
92%	1.69 (Ant)	6.21	0.14	1.18	1.17

<sup>a</sup> CI < 0.9, (0.9–1.1), and >1.1 indicate synergism (Syn), additive effect (Add), and antagonism (Ant), respectively. Fa signifies fraction affected. DRI > 1 indicates favourable dose reduction (in fold) for the drug in combination.

Table 10 revealed that the combination treatment of rosmarinic acid and febuxostat synergistically diminished XO activity with favorable dose reduction compared to individual compound treatment. Combination analysis demonstrated that the CI

values at 10%, 30% and 50% effect levels are consistently below 1, indicating synergy (Table 10) and subsequently, their corresponding combination data points were located below the line of additivity in the isobologram (Fig. 12D) whereas the

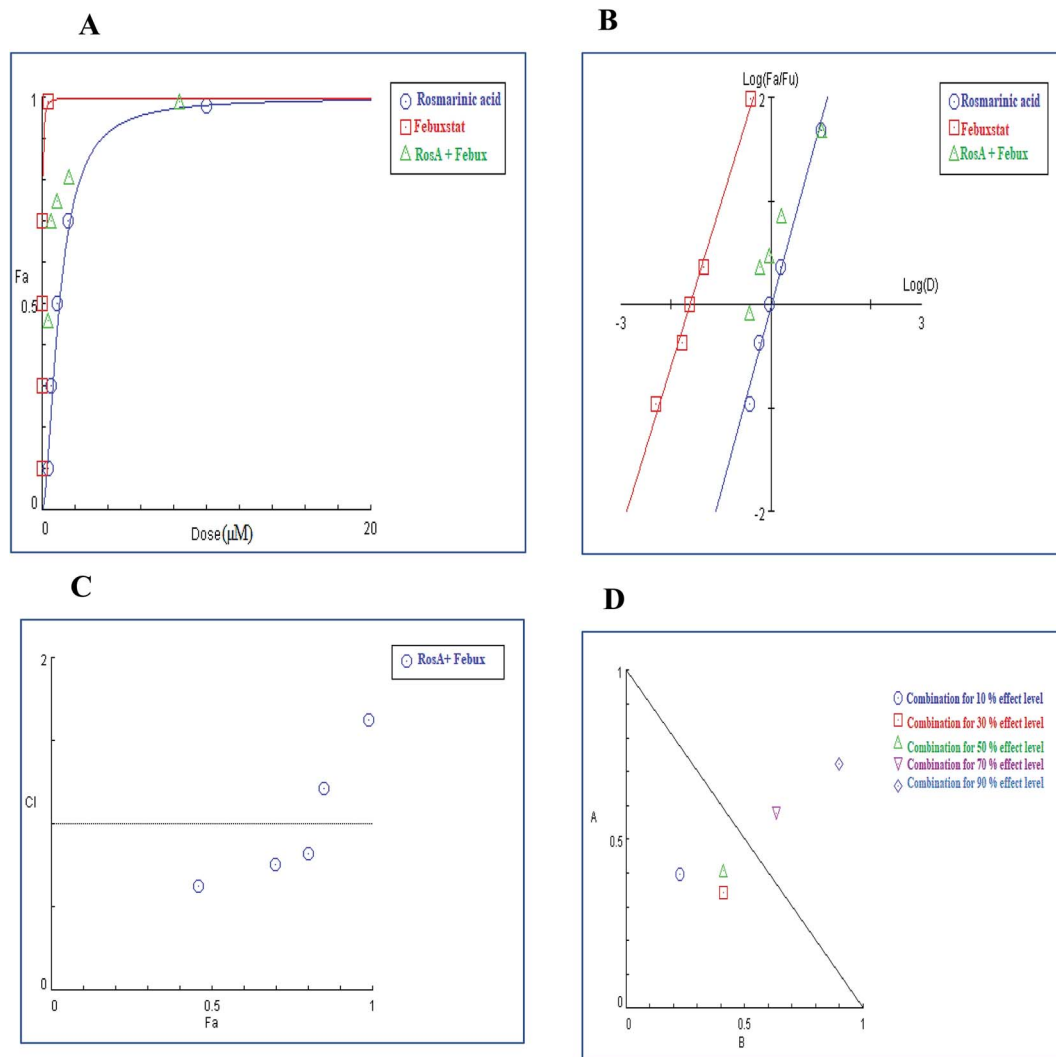


**Fig. 12** Combination analysis of rosmarinic acid and febuxostat; (A) Dose-effect curve and its linearization with the (B) median-effect plot for a single and combination treatment (C) combination index plot. (D) Dose-normalized isobologram for several effects (10%, 30%, 50%, 70 and 90%) in the combinations of rosmarinic acid and febuxostat.



**Table 11** Fractional inhibition of XO, combination index (CI) values and DRI values of rosmarinic acid and allopurinol in combination dose at different effect levels<sup>a</sup>

(Fa × 100)% (XO) inhibition of the combined drugs	CI values	Dose (μM) rosmarinic acid	Dose (μM) allopurinol	DRI rosmarinic acid	DRI allopurinol
16%	1.66 (Ant)	0.32	0.23	1.14	1.28
34%	1.43 (Ant)	0.72	0.54	1.49	1.29
69%	0.96 (Add)	2.06	1.61	2.12	1.96
93%	0.56 (Syn)	8.35	6.80	3.42	3.70
98%	0.47 (Syn)	21.32	17.89	4.08	4.41

<sup>a</sup> CI < 0.9, (0.9–1.1), and >1.1 indicate synergism (Syn), additive effect (Add), and antagonism (Ant), respectively. Fa signifies fraction affected. DRI > 1 indicates favourable dose reduction (in fold) for the drug in combination.

combination index at 70% and 90% inhibition effect levels (Fig. 12C) readily represented moderate antagonism with IC values of 1.31 and 1.69, respectively (Table 10).

Our experimental data suggested that the combination of rosmarinic acid and febuxostat at low dose levels displayed a better synergistic effect than at high doses. This fact pointed out that the synergistic interactions might be weakened and

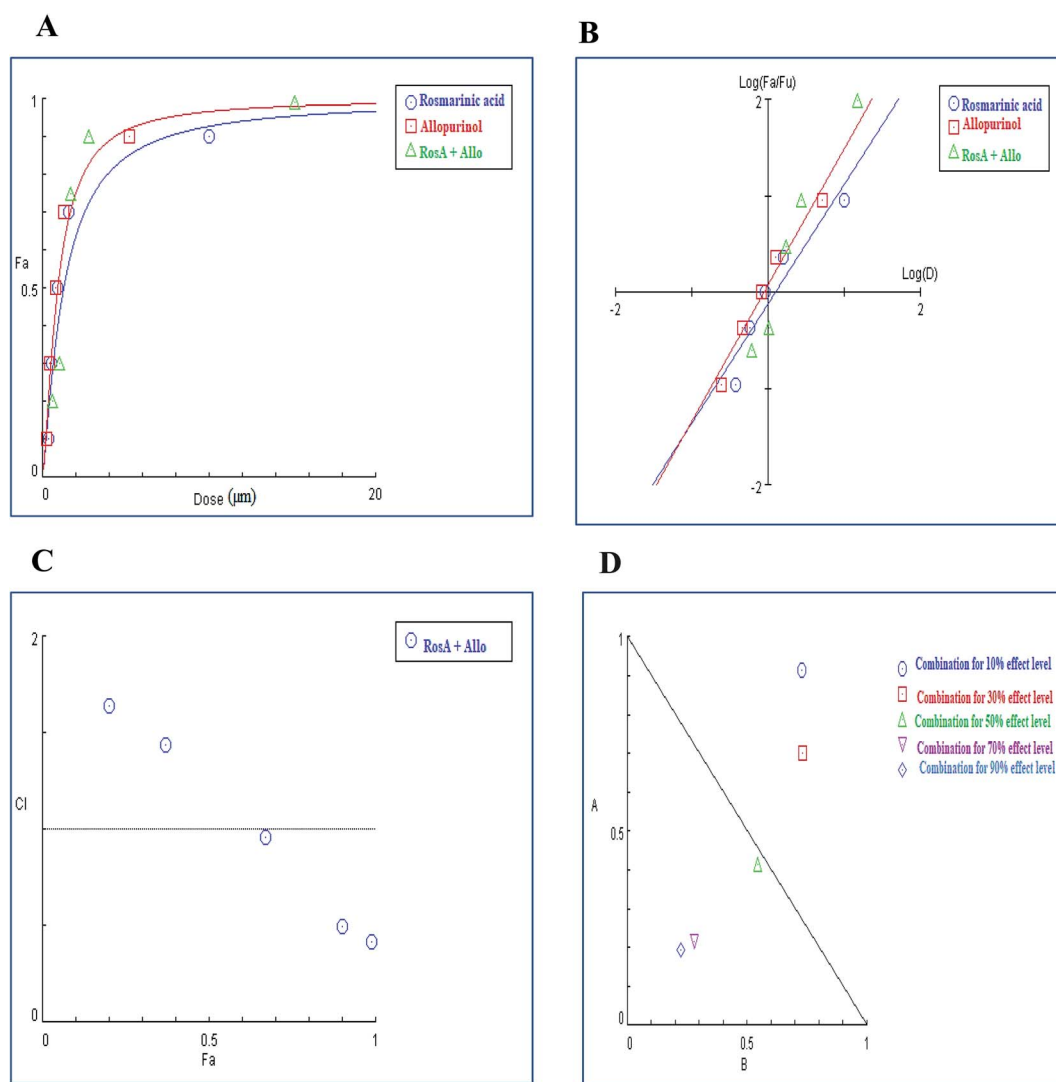


**Fig. 13** Combination analysis of rosmarinic acid and allopurinol; (A) dose-effect curve and its linearization with the (B) median-effect plot for a single and combination treatment (C) combination index plot. (D) Dose-normalized isobologram for several effects (10%, 30%, 50%, 70 and 90%) in the combinations of rosmarinic acid and allopurinol.



**Table 12** Summary table showing potency ( $Fa \times 100$ ), CI and DRI values of febuxostat and techtochrysin combined at various concentrations and ratios<sup>a</sup>

Fa × 100 (%) (CI) DRI febuxostat DRI techtochrysin		Techtochrysin (μM)					
		0	0.021	0.042	0.084	0.168	0.336
Febuxostat (μM)	0	0%	8%	22%	50%	64%	78%
	0.0025	6%	30%	46%	62%	72%	78%
			0.41	0.44	0.52	0.66	0.96
			8.51	11.01	18.67	90.61	121.92
	0.005	10%	2.58	2.17	1.43	1.38	0.93
			43%	53%	63%	69%	79%
			0.48	0.58	0.62	0.79	1.11
	0.01	24%	3.82	4.2	9.78	13.9	70.71
			3.89	2.23	1.97	1.18	1.02
			58%	66%	71%	77%	84%
	0.02	50%	0.57	0.62	0.76	0.85	1.12
			3.85	3.66	3.7	7.93	11.88
			5.03	3.34	2.04	1.64	1.12
	0.04	70%	62%	70%	76%	80%	90%
			0.68	0.73	0.78	0.89	1.13
			3.36	2.03	3.04	2.99	6.54
	0.04	70%	3.92	3.66	2.72	1.7	1.38
			73%	79%	84%	89%	93%
			0.95	0.98	1.02	0.99	0.96
	0.04	70%	1.81	1.21	2.66	2.43	2.62
			2.66	3.62	1.42	2.11	1.61

<sup>a</sup> The molar febuxostat–techtochrysin ratios 1 : 2.1, 1 : 4.2 ( $IC_{50} : IC_{50}$  ratio), 1 : 8.4, 1 : 16.8, and 1 : 33.6 are indicated in pink, green ( $IC_{50} : IC_{50}$  ratio), red, orange and grey, respectively.

even converted into antagonistic interactions with a higher dose, then bringing about undesirable adverse effects. In the same context, rosmarinic acid and allopurinol cooperated synergistically at high dose levels yielding XO inhibition that was greater than the expected inhibition achieved by either agent alone (Table 11).

Isobologram demonstrated a stark reduction of the allopurinol dose when used with rosmarinic acid to induce even 50% inhibition or greater (Fig. 13D). In combination, allopurinol could be used at a concentration 4.41-fold less compared to its single-use to inhibit XO by 98% (Table 11). This observation

agreed with data from CI plots showing antagonism below 50% inhibition level and synergy above 50% effect level (Fig. 13C). The calculated CI value at 50% effect level was 0.96 and its corresponding combination data point was located around the horizontal line of additivity in the CI-plot (Fig. 13C). The separation of the experimental points in the CI-plot was consistent with that in the isobologram. Briefly, CI decreased with increasing effect levels, indicating the enhancement of the extent of synergy at higher effect levels.

**3.4.3. Multiple ratio combinations of febuxostat and techtochrysin.** As mentioned above, the effectiveness of



combination therapy is not simply due to the properties of the drugs, but also depends on the dose ratio. Two drugs combined at a particular ratio might be regarded as a third drug with its own concentration-effect relation, certain ratios of combined drugs could be synergistic, while other ratios of the same drugs could be merely additive or even antagonistic. Hence, rather than simply asking whether a specific combination is synergistic, we should do better to realize what dose ratios optimize the synergistic actions. Keeping in mind the above facts, a multiple-ratio design for febuxostat and techtochrysin combination was established for controlling the optimal drug dose ratios to exploit synergistic effect more effectively and avoid antagonistic interactions, thus has paved the way for gathering the maximal therapeutic efficacy with lower doses to minimize potential toxicity in the combination therapy of gout.

The multiple-ratio analysis elicited a broad range of the inhibitory effect level [e.g., ranging from less than 10% to greater than 90% inhibition of XO]. Among the full range of 25 combinations, calculated CI values ( $<0.9$ ) indicated that the combination of febuxostat and techtochrysin at the effect level 50% or lower provided the maximal synergistic effect (Table 12). Notably, the molar concentration ratios (1 : 2.1 and 1 : 4.2 ( $IC_{50} : IC_{50}$  ratio)) that contained higher relative amounts of febuxostat displayed lower synergy compared with that of lower febuxostat doses (1 : 8.4, 1 : 16.8, and 1 : 33.6), which yielded good synergistic effect especially at lower effect levels. Additionally, the required dose levels of febuxostat in the combination are substantially reduced as techtochrysin dose levels increase. This decline in dose level also referred to as dose reduction index (DRI) (Table 12) might be most relevant for gout treatment.

Further supportive evidence for the synergistic action of these ratios was obtained from curve-shift analyses, which readily circumvented the interaction analysis across the entire spectrum of effect levels and statistically estimated the effect deviation of combined agents from additivity. Curve-shift analysis pointed out that all concentration-effect curves for different techtochrysin and febuxostat ratio combinations were

situated to the left of the curves for the two individual drugs. Furthermore, pronounced lower  $IC_{50}$  equivalents of the combination compared with  $IC_{50}$  values of single drugs alone were observed as a read-out of synergy (Fig. 14). The  $IC_{50}$  equivalents ranged from 0.2 to 0.82  $\mu\text{M}$  for all combination ratios at 50% effect level with the corresponding extent of synergy ranging from approximately 1.5 to 8-fold leftward shifts along the x-axis in the curve-shift plot at this level (Fig. 14).

The data presented herein outlined that the febuxostat plus techtochrysin combination at molar concentration ratios (1 : 8.4, 1 : 16.8, and 1 : 33.6) at lower effect levels were particularly effective with prominent XO inhibitory activity and simultaneous lower toxicity profile compared to those of the single drugs. It is also important to highlight that the results of the *in vitro* combination analysis studies matched very well with the outcomes of the molecular docking studies and MD simulations (Sections 3.1 and 3.3) and validated these computer-directed studies.

## 4. Conclusion

In summary, Egyptian propolis-derived bioactive primarily techtochrysin and rosmarinic acid were found to be the most promising XO inhibitory hits for further development. Docking and MD simulations provided putative binding modes within the XO active site, which could intuitively illustrate the postulated potential observed for techtochrysin and rosmarinic acid on XO catalysis. A cooperative binding mode has been proposed between techtochrysin and standard XO inhibitors such as febuxostat and this cooperativity was supported by MD simulation studies. Future fluorescence spectroscopic studies and circular dichroism analysis should be conducted to provide additional insights on conformational changes in XO structure upon techtochrysin binding. Additionally, the combination of techtochrysin and rosmarinic acid with each of febuxostat and allopurinol synergistically inhibited XO activity with favorable dose reduction of synthetic drugs. Besides, the optimization of dose ratios in the investigated combination regimens has been conducted. However, further *in vivo* studies are required to confirm the superior activity of the proposed combination and consider its influence on blood biochemistry profile as well as at the histological and molecular levels, thus revealing its therapeutic mechanism in hyperuricemia and gout at the overall level.

## Author contributions

Dina S. Ghallab: carrying out the experiments and writing the manuscript, dodoghalab3@gmail.com; Eman Shawky: designing the experiments and manuscript revision, shawkyeman@yahoo.com; Ali M. Metwally: suggesting point and manuscript revision, alymmetwally@yahoo.com; Ismail Celik: performing and writing the molecular dynamic simulation. Reham S. Ibrahim: analysis of data and manuscript revision, rehamsaid84@yahoo.com; Mohamed M. Mohyeldin: analysis of data and manuscript revision, mo7yee@hotmail.com.

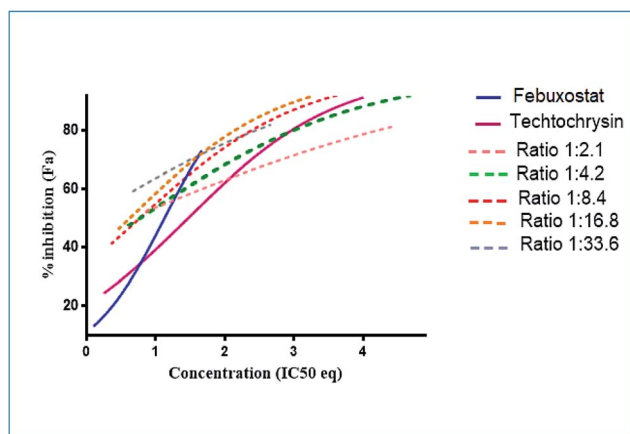


Fig. 14 Curve shift analysis of various drug ratios. The molar febuxostat–techtochrysin ratios 1 : 2.1, 1 : 4.2 ( $IC_{50} : IC_{50}$  ratio), 1 : 8.4, 1 : 16.8, and 1 : 33.6 are indicated in pink, green ( $IC_{50} : IC_{50}$  ratio), red, orange and grey, respectively.



## Conflicts of interest

We wish to confirm that there are no known conflicts of interest associated with this publication and there has been no significant financial support for this work that could have influenced its outcome.

## Acknowledgements

All molecular dynamics simulations reported were performed utilizing TÜBİTAK (The Scientific and Technological Research Council of Turkey), ULAKBİM (The Turkish Academic Network and Information Center), and High Performance and Grid Computing Center (TRUBA resources).

## References

- 1 A. Šmelcerović, K. Tomović, Ž. Šmelcerović, Ž. Petronijević, G. Kocić, T. Tomašić, Ž. Jakopin and M. Anderluh, *Eur. J. Med. Chem.*, 2017, **135**, 491–516.
- 2 J. Labat-Robert and L. Robert, *Pathol. Biol.*, 2014, **62**, 61–66.
- 3 R. Tanaka, Y. Miyata, N. Minakuchi, A. Murakami and F. Sakazaki, *Yakugaku Zasshi*, 2015, **135**, 1169–1176.
- 4 C. Enroth, B. T. Eger, K. Okamoto, T. Nishino, T. Nishino and E. F. Pai, *Proc. Natl. Acad. Sci. U. S. A.*, 2000, **97**, 10723–10728.
- 5 H. K. Choi, D. B. Mount and A. M. Reginato, *Ann. Intern. Med.*, 2005, **143**, 499–516.
- 6 P. Zhao, K. Chen, G. Zhang, G. Deng and J. Li, *J. Evidence-Based Complementary Altern. Med.*, 2017, DOI: 10.1155/2017/2103254.
- 7 P. Richette, A. Frazier and T. Bardin, *Curr. Opin. Rheumatol.*, 2015, **27**, 170–174.
- 8 E. Fadillioglu, Z. Kurcer, H. Parlakpinar, M. Iraz and C. Gursul, *Arch. Pharmacol. Res.*, 2008, **31**, 705–712.
- 9 P. A. L. Pacher, A. Nivorozhkin and C. Szabó, *Pharmacol. Rev.*, 2006, **58**, 87–114.
- 10 P. A. L. Pacher, A. Nivorozhkin and C. Szabó, *Pharmacol. Rev.*, 2006, **58**, 87–114.
- 11 A. Jordan and U. Gresser, *Pharmaceuticals*, 2018, **11**, 51.
- 12 A. Jordan and U. Gresser, *Pharmaceuticals*, 2018, **11**, 51.
- 13 A. M. Abeles and M. H. Pillinger, *ACR Open Rheumatology*, 2019, **1**, 343.
- 14 S. Bogdanov, *Bee Product Science*, 2014, 1–40.
- 15 P. Ristivojević, J. Trifković, F. Andrić and D. Milojković-Opsenica, *Nat. Prod. Commun.*, 2015, **10**(11), 1869–1876.
- 16 V. S. Bankova, S. S. Popov and N. L. Marekov, *Phytochemistry*, 1989, **28**, 871–873.
- 17 B. Meyer, W. Schneider and E. F. Elstner, *Arzneim. Forsch.*, 1995, **45**, 174–176.
- 18 B. Meyer, W. Schneider and E. F. Elstner, *Arzneim. Forsch.*, 1995, **45**, 174–176.
- 19 N. Debbache, D. Atmani and D. Atmani, *Ind. Crops Prod.*, 2014, **53**, 85–92.
- 20 V. Bankova, *Journal of ApiProduct and ApiMedical Science*, 2009, **1**, 23–28.
- 21 A. G. Hegazi, A. S. El-Houssiny and E. A. Fouad, *Adv. Nat. Sci.: Nanosci. Nanotechnol.*, 2019, **10**, 45019.
- 22 E. Shawky and R. S. Ibrahim, *J. Chromatogr. B: Anal. Technol. Biomed. Life Sci.*, 2018, **1095**, 75–86.
- 23 N. Baltas, O. Yildiz and S. Kolayli, *J. Enzyme Inhib. Med. Chem.*, 2016, **31**, 52–55.
- 24 M. D. Santi, M. P. Zunini, B. Vera, C. Bouzidi, V. Dumontet, A. Abin-Carriquiry, R. Grougnet and M. G. Ortega, *Eur. J. Med. Chem.*, 2018, **143**, 577–582.
- 25 Y. Dong, H. Huang, M. Zhao, D. Sun-Waterhouse, L. Lin and C. Xiao, *J. Funct. Foods*, 2016, **24**, 26–36.
- 26 E. Lionta, G. Spyrou, D. K. Vassilatis and Z. Cournia, *Curr. Top. Med. Chem.*, 2014, **14**, 1923–1938.
- 27 J. R. Pritchard, P. M. Bruno, L. A. Gilbert, K. L. Capron, D. A. Lauffenburger and M. T. Hemann, *Proc. Natl. Acad. Sci. U. S. A.*, 2013, **110**, E170–E179.
- 28 J. Fouquier and M. Guedj, *Pharmacol. Res. Perspect.*, 2015, **3**, e00149.
- 29 J. Fouquier and M. Guedj, *Pharmacol. Res. Perspect.*, 2015, **3**, e00149.
- 30 R. B. Mokhtari, T. S. Homayouni, N. Baluch, E. Morgatskaya, S. Kumar, B. Das and H. Yeger, *Oncotarget*, 2017, **8**, 38022.
- 31 B. Sillars, W. A. Davis, I. B. Hirsch and T. M. E. Davis, *Diabetes, Obes. Metab.*, 2010, **12**, 757–765.
- 32 N. Zeng, G. Zhang, X. Hu, J. Pan, Z. Zhou and D. Gong, *J. Funct. Foods*, 2018, **50**, 172–182.
- 33 K. E. Hevener, W. Zhao, D. M. Ball, K. Babaoglu, J. Qi, S. W. White and R. E. Lee, *J. Chem. Inf. Model.*, 2009, **49**, 444–460.
- 34 M. J. Abraham, T. Murtola, R. Schulz, S. Páll, J. C. Smith, B. Hess and E. Lindahl, *SoftwareX*, 2015, **1–2**, 19–25.
- 35 S. Jo, T. Kim, V. G. Iyer and W. Im, *J. Comput. Chem.*, 2008, **29**, 1859–1865.
- 36 C. Tian, K. Kasavajhala, K. A. A. Belfon, L. Raguette, H. Huang, A. N. Miguez, J. Bickel, Y. Wang, J. Pincay, Q. Wu and C. Simmerling, *J. Chem. Theory Comput.*, 2020, **16**, 528–552.
- 37 D. J. Evans and B. L. Holian, *J. Chem. Phys.*, 1985, **83**, 4069–4074.
- 38 M. Parrinello and A. Rahman, *J. Appl. Phys.*, 1981, **52**, 7182–7190.
- 39 R. Kumari, R. Kumar and A. Lynn, *J. Chem. Inf. Model.*, 2014, **54**, 1951–1962.
- 40 L. Zhao, M. G. Wientjes and J. L. S. Au, *Clin. Cancer Res.*, 2004, **10**, 7994–8004.
- 41 L. Zhao, M. G. Wientjes and J. L. S. Au, *Clin. Cancer Res.*, 2004, **10**, 7994–8004.
- 42 T.-C. Chou, *Pharmacol. Rev.*, 2006, **58**, 621–681.
- 43 T.-C. Chou, *Pharmacol. Rev.*, 2006, **58**, 621–681.
- 44 I. Rodea-Palomares, A. L. Petre, K. Boltes, F. Leganés, J. A. Perdigón-Melón, R. Rosal and F. Fernández-Piñas, *Water Res.*, 2010, **44**, 427–438.
- 45 I. Rodea-Palomares, A. L. Petre, K. Boltes, F. Leganés, J. A. Perdigón-Melón, R. Rosal and F. Fernández-Piñas, *Water Res.*, 2010, **44**, 427–438.
- 46 J. Zhao, K. Kelnar and A. G. Bader, *PLoS One*, 2014, **9**, e89105.
- 47 J. Zhao, K. Kelnar and A. G. Bader, *PLoS One*, 2014, **9**, e89105.
- 48 L. Zhao, J. L.-S. Au and M. G. Wientjes, *Front. Biosci., Elite Ed.*, 2010, **2**, 241.



- 49 C. Enroth, B. T. Eger, K. Okamoto, T. Nishino, T. Nishino and E. F. Pai, *Proc. Natl. Acad. Sci. U. S. A.*, 2000, **97**, 10723–10728.
- 50 H. Cao, J. M. Pauff and R. Hille, *J. Nat. Prod.*, 2014, **77**, 1693–1699.
- 51 H. Cao, J. M. Pauff and R. Hille, *J. Nat. Prod.*, 2014, **77**, 1693–1699.
- 52 L. Fitria, M. H. Widyananda and S. P. Sakti, *Journal of Smart Bioprospecting and Technology*, 2019, **2686**, 805.
- 53 L. Fitria, M. H. Widyananda and S. P. Sakti, *Journal of Smart Bioprospecting and Technology*, 2019, **2686**, 805.
- 54 J. Yan, G. Zhang, Y. Hu and Y. Ma, *Food Chem.*, 2013, **141**, 3766–3773.
- 55 M. D. Santi, M. P. Zunini, B. Vera, C. Bouzidi, V. Dumontet, A. Abin-Carriquiry, R. Grougnet and M. G. Ortega, *Eur. J. Med. Chem.*, 2018, **143**, 577–582.
- 56 M. R. Ali, S. Kumar, O. Afzal, N. Shalmali, W. Ali, M. Sharma and S. Bawa, *Arch. Pharm.*, 2017, **350**, 1600313.
- 57 D. Sato, T. Kisen, M. Kumagai and K. Ohta, *Bioorg. Med. Chem.*, 2018, **26**, 536–542.
- 58 D. Sato, T. Kisen, M. Kumagai and K. Ohta, *Bioorg. Med. Chem.*, 2018, **26**, 536–542.
- 59 J. Yun, J. Mattsson, K. Schnyder, S. Fontana, C. R. Largiadèr, W. J. Pichler and D. Yerly, *Clin. Exp. Allergy*, 2013, **43**, 1246–1255.
- 60 W. Choi, V. Villegas, H. Istre, B. Heppler, N. Gonzalez, N. Brusman, L. Snider, E. Hogle, J. Tucker and A. Oñate, *Bioorg. Chem.*, 2019, **86**, 686–695.
- 61 H. Zhao and A. Caflisch, *Eur. J. Med. Chem.*, 2015, **91**, 4–14.
- 62 I. Celik, M. Erol and Z. Duzgun, *Mol. Diversity*, 2021, DOI: 10.1007/s11030-021-10215-5.
- 63 I. Celik, M. Erol and G. Kuyucuklu, *New J. Chem.*, 2021, **45**, 11108–11118.
- 64 M. Erol, I. Celik, U. Ince, H. Fatullayev, E. Uzunhisarcikli and M. O. Puskullu, *J. Biomol. Struct. Dyn.*, 2021, 1–15.
- 65 N. Homeyer and H. Gohlke, *Mol. Inf.*, 2012, **31**, 114–122.

